changes in AD are deposition of amyloid senile plaques and neurofibrillary tangles (NFTs) [1]. The amyloid cascade hypothesis that deposition of amyloid protein would cause Alzheimer's pathology, e.g., the NFTs, cell loss, and vascular damage as a direct result of this deposition, has been proposed [2], and in vivo imaging of the deposition of amyloid senile plaques should contribute to the early diagnosis and evaluation for the treatment of AD. Several radiotracers to measure deposition of amyloid senile plaques by positron emission tomography (PET), e.g., [^{11}C]Pittsburgh compound B (PIB) [3, 4], [^{18}F]FDDNP [5], [^{11}C]SB-13 [6], [^{11}C]BF227 [7], [^{18}F]BAY94-9172 [8], [^{18}F]AV-45 [9], [^{11}C]AZD2184 [10], and [^{18}F]AZD4694 [11], were developed and used for investigation of the pathophysiology of AD.

[^{11}C]PIB, a benzothiazole derivative, is the most successful radiotracer for amyloid imaging and is widely used for clinical research of AD [12, 13]. However, cortical uptake of [^{11}C]PIB was often observed in healthy subjects with normal neuropsychological findings [14]. Since the fraction of soluble amyloid deposition in normal brain has been reported to be larger than that in AD brain [15], the cortical uptake of [^{11}C]PIB in normal subjects might be mainly due to binding to diffuse amyloid plaque.

Recently, [^{11}C]BF227, a benzoxazole derivative, was developed for in vivo imaging of amyloid senile plaques [7]. This radiotracer has been considered to bind more preferentially to dense-cored amyloid deposition than [^{11}C]PIB. It has been reported that synapse loss was accentuated within immature and mature plaques, but not within diffuse plaques [16], and the neuropathology of AD is characterized by cortical neuritic plaque containing dense-cored amyloid deposition [17]. Thus, a selective radiotracer for neuritic amyloid plaque might be useful for distinguishing the normal aging process from AD.

The ^{18}F-labeled amyloid tracer, [^{18}F]2-[(2-{(E)-2-[2-(dimethylamino)-1,3-thiazol-5-yl]vinyl}-1,3-benzoxazol-6-yl)oxy]-3-fluoropropan-1-ol (fluorinated amyloid imaging compound of Tohoku University, [^{18}F]FACT), one of the benzoxazole derivatives with a structure similar to [^{11}C]BF227, was recently developed [18, 19]. For [^{18}F]FACT, rapid accumulation and rapid washout were observed in the brains of both normal control subjects and AD patients, indicating its suitability as an amyloid imaging tracer in PET measurements [18]. Regional distribution similar to that of [^{11}C]BF227 was also observed. In the present study, deposition of amyloid senile plaques was measured by PET with both [^{11}C]PIB and [^{18}F]FACT in the same subjects including normal control subjects, mild cognitive impairment (MCI) patients, and AD patients. The binding and regional distribution of both radiotracers were directly compared to elucidate the binding characteristics of [^{18}F]FACT. To identify pathological aggregates providing major binding components for [^{11}C]PIB and [^{18}F]FACT, comparative autoradiographic and histochemical assays of postmortem AD brain sections were also performed.

Materials and methods

Subjects

Six normal control subjects (50–74 years old), two MCI patients (69 and 77 years old), and six AD patients (70–81 years old) were recruited (Table 1). All AD patients were diagnosed according to the National Institute of Neurological and Communicative Diseases and Stroke/Alzheimer's Disease and Related Disorders Association (NINCDS-ADRDA) criteria [20]. All subjects were classified according to the Clinical Dementia Rating (CDR) scale [21]. The normal control subjects corresponded to 0, the MCI patients to 0.5, and the AD subjects to 0.5, 1, or 2 on the CDR scale. The Mini-Mental State Examination (MMSE) was performed for all subjects [22]. No subjects had notable organic lesions in the brain according to magnetic resonance (MR) imaging. The normal control subjects were cognitively unimpaired and free from medications having central nervous action. The study was approved by the Ethics and Radiation Safety Committees of the National Institute of Radiological Sciences, Chiba, Japan. Written informed consent was obtained from all subjects or from their spouses or other close family members.

PET procedures

All PET studies were performed with SET-3000GCT/X (Shimadzu Corp., Kyoto, Japan) [23], which provides 99

Table 1 Profiles of subjects

Subject group	Subject no.	Age (years)	Sex	MMSE score
Normal control	NC1	70	F	29
	NC2	73	M	29
	NC3	74	M	29
	NC4	50	M	28
	NC5	61	M	28
	NC6	67	F	30
MCI	MCI1	77	F	26
	MCI2	69	M	24
AD	AD1	76	F	12
	AD2	71	M	19
	AD3	81	F	19
	AD4	70	F	15
	AD5	76	F	22
	AD6	80	F	24

sections with an axial field of view of 26 cm. Intrinsic spatial resolution was 3.4 mm in-plane and 5.0 mm full-width at half-maximum (FWHM) axially. With a Gaussian filter (cutoff frequency: 0.3 cycle/pixel), the reconstructed in-plane resolution was 7.5 mm FWHM. Data were acquired in three-dimensional mode. Scatter correction was done by a hybrid scatter correction method based on acquisition with a dual-energy window setting [24]. A 4-min transmission scan using a ^{137}Cs line source was performed for correction of attenuation.

Two PET scans, one each with [^{11}C]PIB and [^{18}F]FACT, were performed sequentially. After intravenous rapid bolus injection of [^{11}C]PIB, dynamic PET scanning was performed for 70 min. Then, 50 min after the end of the [^{11}C]PIB PET measurement, dynamic PET scanning was performed for 60 min after intravenous rapid bolus injection of [^{18}F]FACT. The frame sequence consisted of six 10-s frames, three 20-s frames, two 1-min frames, two 3-min frames, and twelve 5-min frames for [^{11}C]PIB and six 10-s frames, three 20-s frames, two 1-min frames, two 3-min frames, and ten 5-min frames for [^{18}F]FACT. Injected radioactivity was 332–493 MBq and 160–233 MBq for [^{11}C]PIB and [^{18}F]FACT, respectively. Specific radioactivity was 51–134 GBq/μmol and 59–494 GBq/μmol for [^{11}C]PIB and [^{18}F]FACT, respectively. [^{18}F]FACT was produced according to the literature [18].

MR imaging procedures

All MR imaging studies were performed with a 1.5-T MR scanner (Philips Medical Systems, Best, The Netherlands). Three-dimensional volumetric acquisition of a T1-weighted gradient echo sequence produced a gapless series of thin transverse sections (echo time 9.2 ms, repetition time 21 ms, flip angle 30°, field of view 256 mm, acquisition matrix 256 × 256, slice thickness 1 mm).

Calculation of parametric images

For both [^{11}C]PIB and [^{18}F]FACT studies, standardized uptake value (SUV) images were calculated from time-integrated radioactivity images by normalizing tissue radioactivity concentration with injected dose per body weight. The integration intervals were 50–70 min and 40–60 min for [^{11}C]PIB and [^{18}F]FACT, respectively. Since the cerebellum can be used as a reference brain region lacking fibrillar amyloid plaques [7, 25], the SUV ratio (SUVR) images, indicating amyloid deposition, were calculated as follows:

$$SUVR = SUV_{brain}/SUV_{cerebellum} \quad (1)$$

where SUV_{brain} and $SUV_{cerebellum}$ are SUV in brain regions and the cerebellum, respectively. Although the integration interval of 30–40 min including the peak equilibrium [26] was used for calculation of SUVR in the previous report with [^{18}F]FACT, they showed that almost the same SUVR could be obtained using the integration interval of 40–60 min corresponding to the late time phase after injection of [^{18}F]FACT [18]. Thus, the integration intervals corresponding to the late time phase were used for both [^{11}C]PIB and [^{18}F]FACT in the present study.

Data analysis

All MR images were coregistered to the PET images with the Statistical Parametric Mapping (SPM2) system [27]. MR images were transformed into standard brain size and shape by linear and nonlinear parameters by SPM2 (anatomic standardization). The brain templates used in SPM2 for anatomic standardization were T1 templates for MR images, i.e., Montreal Neurological Institute (MNI)/International Consortium for Brain Mapping (ICBM) 152 T1 templates as supplied with SPM2. All PET images were also transformed into standard brain size and shape by using the same parameters as the MR images. Thus, brain images of all subjects had the same anatomic format. Gray matter, white matter, and cerebrospinal fluid images were segmented and extracted from all anatomically standardized MR images by applying voxel-based morphometry methods with the SPM2 system [28]. These segmented MR images indicate the tissue fraction of gray or white matter per voxel (ml/ml). All anatomically standardized PET, gray matter, and white matter images were smoothed with an 8-mm FWHM isotropic Gaussian kernel, because final spatial resolution of the PET camera was approximately 8 mm FWHM.

Regions of interest (ROIs) were drawn on all anatomically standardized PET, gray matter, and white matter images with reference to the T1-weighted MR image. Elliptical ROIs (8 × 32 mm) were defined for the cerebellar cortex, parahippocampal gyrus including hippocampus, posterior region of the cingulate gyrus, base sides of frontal cortex, lateral side of temporal cortex, parietal cortex, cuneus of occipital cortex, and centrum semiovale.

Partial volume correction

SUV values are affected by the nonspecific accumulation of radiotracer in white matter because of the limited spatial resolution of the PET scanner. The SUV values per gray matter fraction in an ROI for cerebral cortical regions were calculated. The SUV value in an ROI can be expressed as follows [29, 30]:

$$SUV = SUV_{gray} \cdot TF_{gray} + SUV_{white} \cdot TF_{white} \quad (2)$$

where SUV_{gray} and SUV_{white} are SUV in gray and white matter, respectively, and TF_{gray} and TF_{white} are the tissue fraction of gray and white matter (ml/ml), respectively. According to this equation, if SUV_{white} is given, SUV_{gray} can be calculated for a given TF_{gray} and TF_{white}, which are determined by voxel-based morphometry with MR imaging. To correct effects of spill-in and spillover of radioactivity between gray and white matter, gray and white matter images smoothed with an 8-mm FWHM isotropic Gaussian kernel almost the same as the final spatial resolution of the PET camera were used for this partial volume correction. In the present study, the SUV_{gray} values were calculated by assuming SUV_{white} to be equal to the SUV value in the centrum semiovale. From the SUV_{gray} values in brain regions and the cerebellum, SUVR values in gray matter ($SUVR_{gray}$) were calculated by Eq. 1.

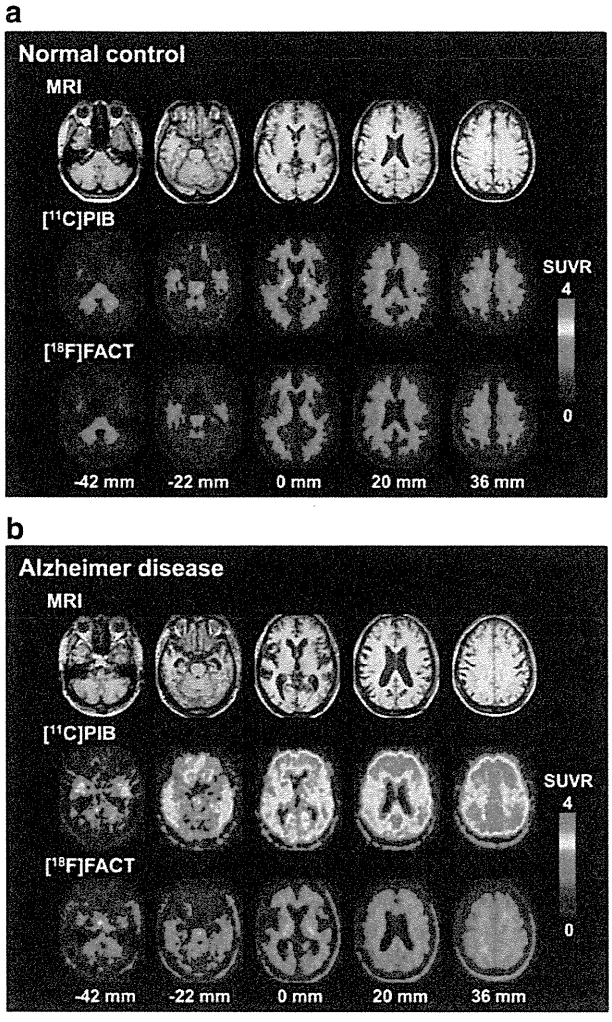

Fig. 1 Typical SUVR images of [^{11}C]PIB and [^{18}F]FACT studies and corresponding MR images (T1-weighted images) for a normal control subject (**a**) and an AD patient (**b**). Scale maximum and minimum values are 4 and 0 of SUVR. All images are transaxial sections parallel to the anterior-posterior commissure (AC-PC) line. Slice positions are −42, −22, 0, 20, and 36 mm from the AC-PC line. Anterior is at the top of the image and the subjects' right is on the left

Table 2 Average SUVR values of [^{11}C]PIB and [^{18}F]FACT studies

Region	[^{11}C]PIB	[^{18}F]FACT
Normal control subjects		
Frontal cortex	1.30±0.13	1.23±0.16
Temporal cortex	1.41±0.11	1.34±0.07
Parietal cortex	1.38±0.11	1.27±0.12
Occipital cortex	1.34±0.17	1.31±0.13
Parahippocampal gyrus	1.46±0.18	1.36±0.10
Posterior cingulate	1.64±0.15	1.49±0.08
Centrum semiovale	2.38±0.31	2.00±0.20
AD patients		
Frontal cortex	2.38±0.61**	1.14±0.13
Temporal cortex	2.14±0.37*	1.27±0.14
Parietal cortex	2.40±0.47*	1.29±0.11
Occipital cortex	1.84±0.27**	1.32±0.12
Parahippocampal gyrus	1.78±0.19***	1.31±0.07
Posterior cingulate	3.03±0.62*	1.61±0.18
Centrum semiovale	2.52±0.33	2.04±0.16

Values are shown as mean ± SD

Significant differences from normal control subjects (unpaired t test): *p <0.001; **p <0.01; ***p <0.05

Table 3 Average SUVR values in gray matter ($SUVR_{gray}$) of [^{11}C]PIB and [^{18}F]FACT studies

Region	[^{11}C]PIB	[^{18}F]FACT
Normal control subjects		
Frontal cortex	1.35±0.23	1.30±0.12
Temporal cortex	1.40±0.12	1.33±0.14
Parietal cortex	1.40±0.18	1.30±0.16
Occipital cortex	1.15±0.13	1.22±0.14
Parahippocampal gyrus	1.31±0.20	1.20±0.17
Posterior cingulate	1.60±0.25	1.44±0.18
AD patients		
Frontal cortex	4.91±1.63*	1.61±0.39****
Temporal cortex	3.53±0.98*	1.58±0.28****
Parietal cortex	4.57±1.47*	1.59±0.30****
Occipital cortex	3.10±1.28**	1.70±0.47***
Parahippocampal gyrus	2.72±0.58*	1.67±0.44***
Posterior cingulate	5.30±1.40*	2.02±0.43***

Values are shown as mean ± SD

Significant differences from normal control subjects (unpaired t test): *p <0.001; **p <0.01; ***p <0.05; ****p <0.1

Autoradiographic and histochemical assays of postmortem brain slices

Formalin-fixed, paraffin-embedded sections were generated from brains of patients with definite AD (generously provided by Dr. Trojanowski and Dr. Lee, University of Pennsylvania). Six-μm-thick slices were incubated in 50 mM Tris-HCl buffer (pH 7.4) containing 5 % ethanol and [^{11}C]PIB (250 MBq/l, approximately 5 nM) at room temperature for 60 min. Nonspecific binding was determined in the presence of 10 μM of nonradioactive PIB. Following the reaction, the samples were rinsed with ice-cold Tris-HCl buffer twice for 2 min and dipped into ice-cold water for 10 s. The slices were subsequently dried under warm blowing air and contacted to an imaging plate (Fujifilm, Tokyo, Japan) for 2 h. The imaging plate data were scanned with a BAS-5000 system (Fujifilm). The intensity of radioactive signals was measured by MultiGauge® software (Fujifilm). These sections were then

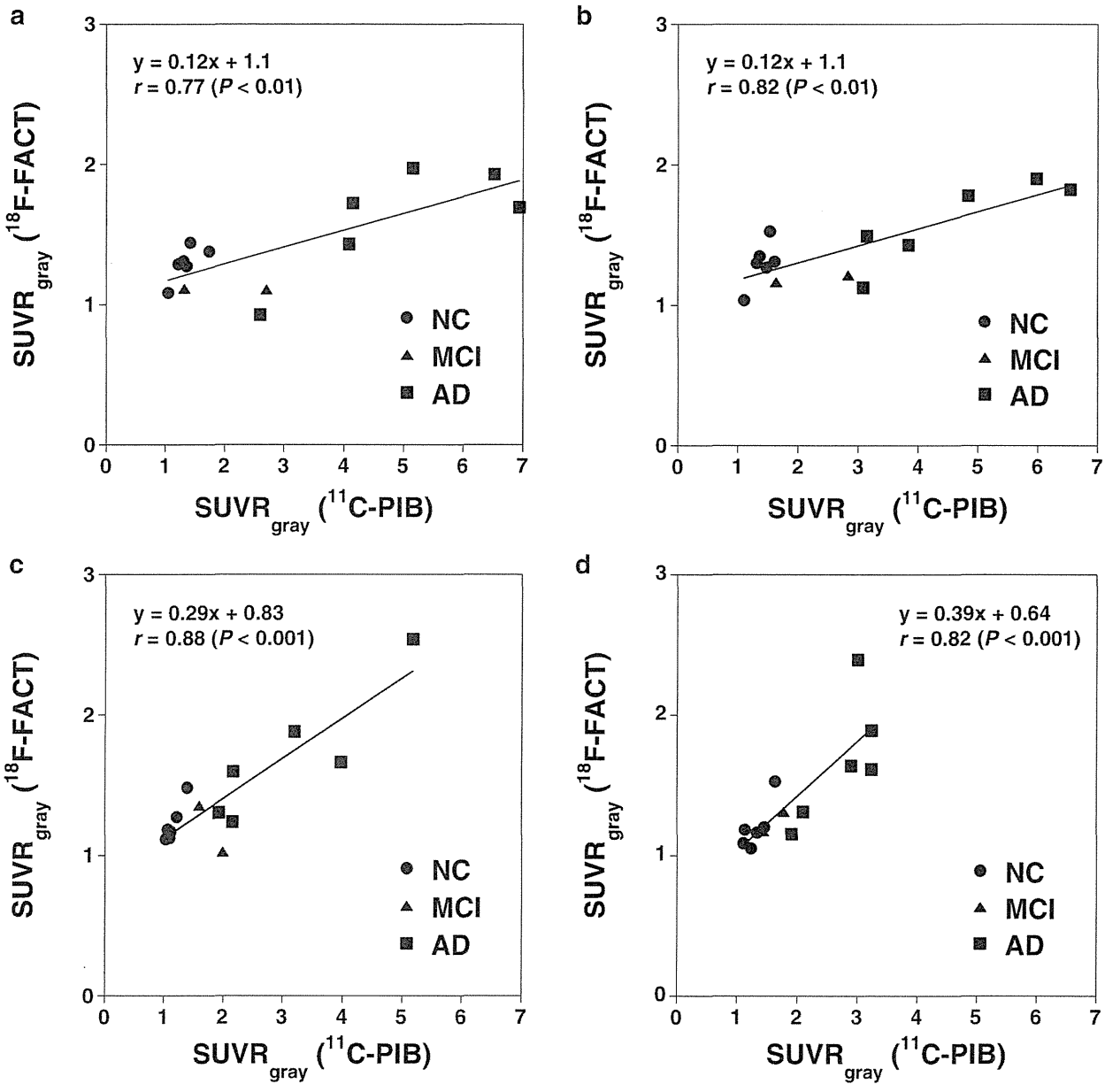

Fig. 2 The relationships of SUVR values in gray matter ($SUVR_{gray}$) between [^{11}C]PIB and [^{18}F]FACT studies for all subjects including normal control subjects (*NC*), mild cognitive impairment patients (*MCI*), and Alzheimer's disease patients (*AD*) in the frontal (**a**), parietal (**b**), occipital cortices (**c**), and parahippocampal gyrus (**d**)

labeled with [^{18}F]FACT 2 weeks after [^{11}C]PIB autoradiography. Briefly, the samples were reacted with [^{18}F]FACT (1 GBq/l, approximately 10 nM) dissolved in a reaction buffer identical to that used for [^{11}C]PIB at room temperature for 60 min. Nonspecific binding was determined in the presence of 10 μM of nonradioactive FACT. Tissue sections were then processed as in [^{11}C]PIB autoradiography and were contacted to an imaging plate for 15 min.

After radioactivity was allowed to decay, brain sections used for the autographic assay were fixed with 4 % paraformaldehyde in phosphate-buffered saline and were stained with 0.01 % (E,E)-1-fluoro-2,5-bis(3-hydroxycarbonyl-4-hydroxy)styrylbenzene (FSB, Dojindo Laboratories, Kumamoto, Japan), a fluorescent amyloid-binding compound, as described elsewhere [31]. Microscopic imaging was performed with an all-in-one microscope/digital camera (BZ-9000, Keyence, Osaka, Japan).

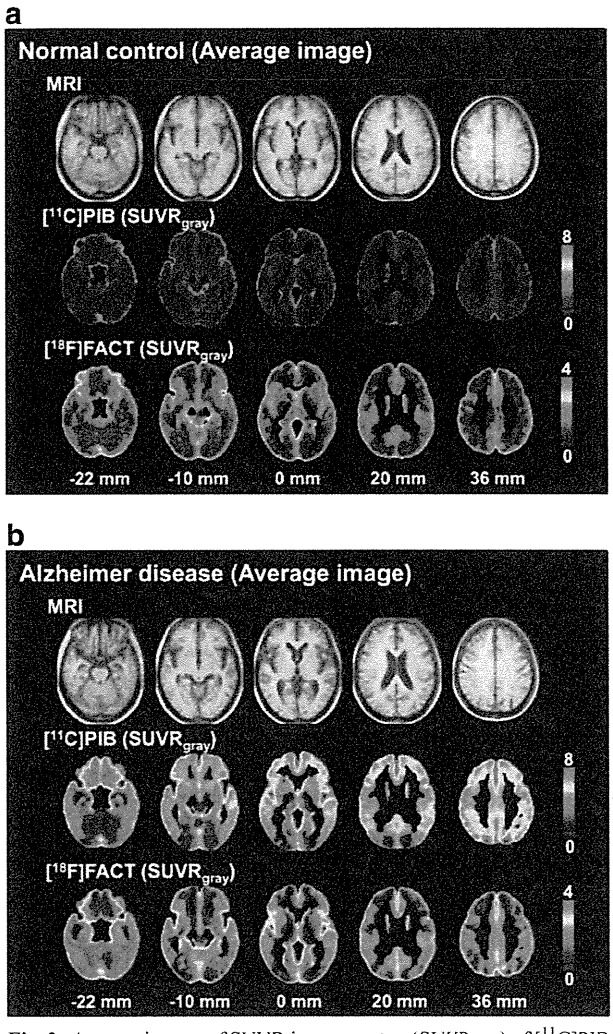

Fig. 3 Average images of SUVR in gray matter ($SUVR_{gray}$) of [^{11}C]PIB and [^{18}F]FACT studies and corresponding average MR images (T1-weighted images) for normal control subjects (**a**) and AD patients (**b**). Scale maximum and minimum values are 8 and 0 of $SUVR_{gray}$ for [^{11}C]PIB and 4 and 0 for [^{18}F]FACT studies. All images are transaxial sections parallel to the anterior-posterior commissure (AC-PC) line. Slice positions are −22, −10, 0, 20, and 36 mm from the AC-PC line. Anterior is at the top of the image and the subjects' right is on the left

Results

Typical SUVR images of [^{11}C]PIB and [^{18}F]FACT studies for a normal control subject are shown in Fig. 1a. Nonspecific accumulation in white matter was observed for both [^{11}C]PIB and [^{18}F]FACT. Typical SUVR images of [^{11}C]PIB and [^{18}F]FACT studies from an AD patient are shown in Fig. 1b. In AD patients, the cortical uptake indicating amyloid deposition was observed for both [^{11}C]PIB and [^{18}F]FACT. In the visual assessment of SUVR images, all normal control subjects and one of the MCI patients were diagnosed as negative for specific accumulation of [^{11}C]PIB, while all AD patients and the other MCI patient were diagnosed as positive.

The SUVR values of [^{11}C]PIB and [^{18}F]FACT studies in normal control subjects and AD patients are shown in Table 2. In [^{11}C]PIB studies, the SUVR values in all cerebral cortical regions were significantly larger in AD patients than in normal control subjects. However, in [^{18}F]FACT studies, no significant differences were observed between normal control subjects and AD patients in any of the brain regions.

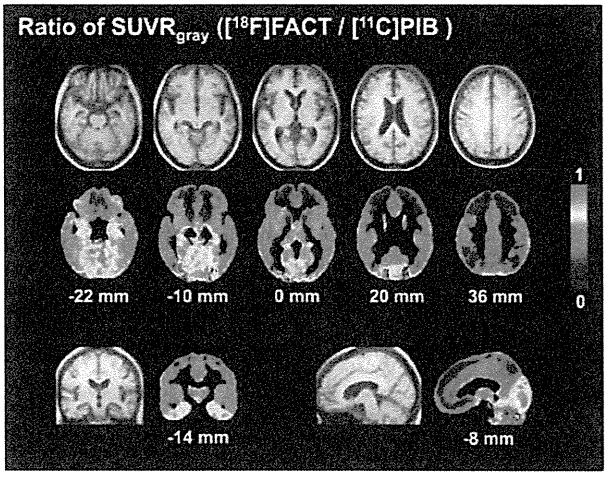

Fig. 4 Average images of ratio of SUVR in gray matter ($SUVR_{gray}$) of [^{18}F]FACT to [^{11}C]PIB studies for AD patients and corresponding average MR images (T1-weighted images). Scale maximum and minimum values are 1 and 0 of ratio. All transaxial images are parallel to the anterior-posterior commissure (AC-PC) line. Slice positions are −22, −10, 0, 20, and 36 mm from the AC-PC line. Anterior is at the top of the image and the subjects' right is on the left. The coronal image is perpendicular to the AC-PC line and its slice position is −14 mm (posterior side) from the AC. The subjects' right is on the left of the image. The sagittal image is parallel to the AC-PC line and its slice position is −8 mm (left side) from the AC-PC line. Anterior is on the left of the image

The $SUVR_{gray}$ values of [^{11}C]PIB and [^{18}F]FACT studies in normal control subjects and AD patients are shown in Table 3. In [^{11}C]PIB studies, the $SUVR_{gray}$ values in all cerebral cortical regions were significantly larger in AD patients than in normal control subjects. In [^{18}F]FACT studies, the $SUVR_{gray}$ value in the occipital cortex, parahippocampal gyrus, and posterior cingulate was significantly larger in AD patients than in normal control subjects. Trends of larger $SUVR_{gray}$ values in AD patients than in normal control subjects were observed in the frontal, temporal, and parietal cortices in the [^{18}F]FACT studies.

The relationships of $SUVR_{gray}$ values between [^{11}C]PIB and [^{18}F]FACT studies for all subjects are shown in Fig. 2. Significant positive correlations were observed in all brain regions. The slopes of linear regression lines (X: [^{11}C]PIB, Y: [^{18}F]FACT) ranged from 0.12 to 0.39. The greatest slopes were observed in the parahippocampal gyrus and occipital cortex, indicating relatively lower $SUVR_{gray}$ of [^{11}C]PIB and relatively higher $SUVR_{gray}$ of [^{18}F]FACT in these regions.

Average images of $SUVR_{gray}$ of [^{11}C]PIB and [^{18}F]FACT studies for normal control subjects and AD patients are shown in Fig. 3. Average images of the ratio of $SUVR_{gray}$ of [^{18}F]FACT to [^{11}C]PIB studies for AD patients are shown in Fig. 4. Relatively lower $SUVR_{gray}$ values of [^{11}C]PIB in distribution were observed in the medial side of the temporal cortex including the parahippocampal gyrus and occipital cortex as compared with [^{18}F]FACT. Relatively higher $SUVR_{gray}$ values of [^{11}C]PIB in distribution were observed in the frontal and parietal cortices.

The relationships between MMSE scores and $SUVR_{gray}$ of [^{11}C]PIB or [^{18}F]FACT studies for all AD patients and the one MCI patient positive for specific accumulation of [^{11}C]PIB are shown in Fig. 5. Significant positive correlations were observed in the temporal cortex for [^{11}C]PIB and in the frontal, parietal, and occipital cortices for [^{18}F]FACT. No significant correlation was observed in the parahippocampal gyrus and posterior cingulate for both [^{11}C]PIB and [^{18}F]FACT.

We then sought to identify pathological aggregates providing major binding components for [^{11}C]PIB and [^{18}F]FACT by comparative autoradiographic and histochemical assays of postmortem AD brain sections. Double autoradiographic labeling demonstrated distinct distribution of binding sites for these two radiotracers (Fig. 6a–c). Radio signals for [^{18}F]FACT were primarily observed in the hippocampal CA1 sector and subiculum besides white matter, in contrast to those for [^{11}C]PIB, which were most intense in the neocortex followed by the parahippocampal gyrus. No noticeable radiolabeling of [^{11}C]PIB and [^{18}F]FACT was detected in the hippocampal CA2 sector harboring numerous NFTs but few plaques (Fig. 6d), while [^{18}F]FACT signals in the CA1 and subiculum appeared to be associated with classic (dense-cored/neuritic) and compact plaques heavily deposited in these areas (Fig. 6e). Diffuse plaques, which were weakly labeled with FSB but involved no overt dystrophic changes of neurites, coexisted with NFTs in the parahippocampal gyrus (Fig. 6f) and therefore could be a source of moderate signals for [^{11}C]PIB. The fusiform gyrus was dominated by coreless

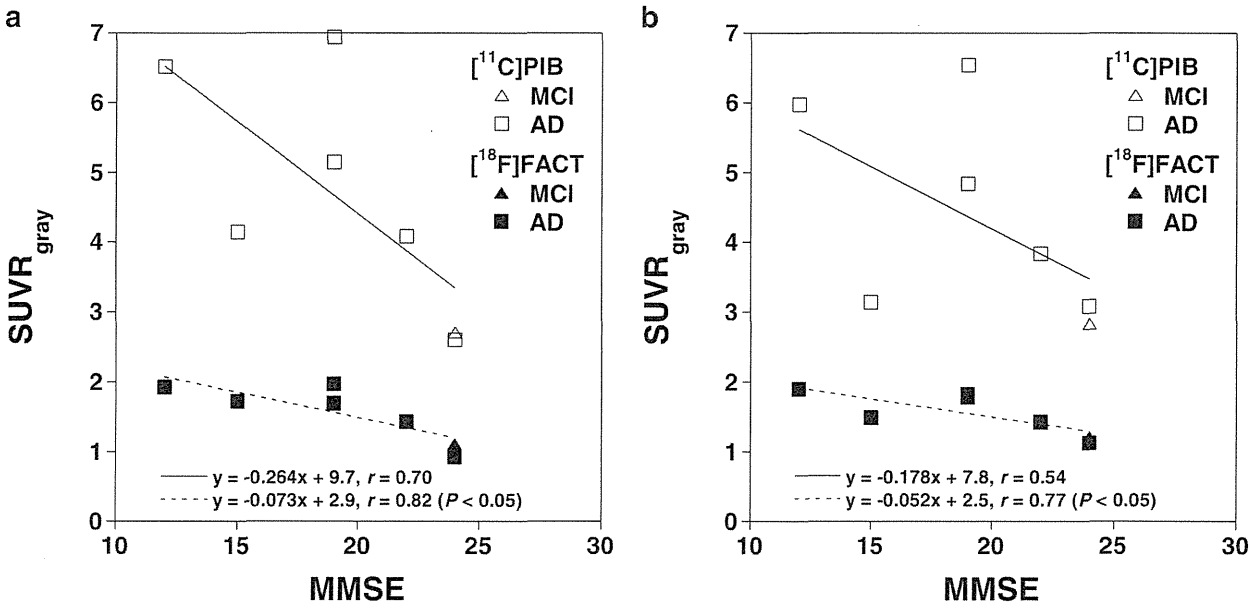

Fig. 5 The relationships between MMSE scores and SUVR values in gray matter ($SUVR_{gray}$) of [^{11}C]PIB or [^{18}F]FACT studies for all Alzheimer's disease patients (*AD*) and one patient with mild cognitive impairment (*MCI*) positive for specific accumulation of [^{11}C]PIB in the frontal (**a**) and parietal cortices (**b**)

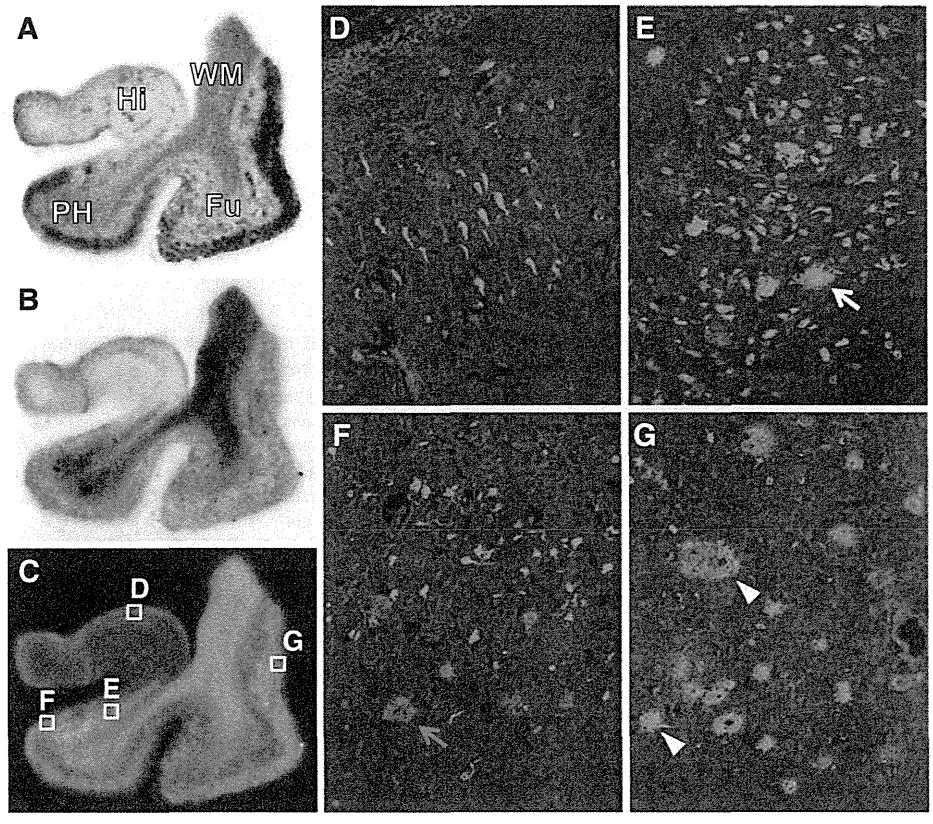

Fig. 6 Binding of [^{11}C]PIB and [^{18}F]FACT to distinct subtypes of senile plaques in AD patient brains. **a**, **b** Autoradiographic labeling of a single AD brain slice with [^{11}C]PIB (**a**) and [^{18}F]FACT (**b**). The section contains the hippocampus (*Hi*), parahippocampal gyrus (*PH*), fusiform gyrus (*Fu*), and white matter (*WM*). **c** Superimposition of autoradiograms displayed in **a** and **b**. *Red* and *green* signals indicate binding of [^{11}C]PIB and [^{18}F]FACT, respectively. *Squares* represent subregions from which photomicrographs shown in **d**–**g** were acquired. **d**–**g** Histofluorescence staining of amyloid lesions with FSB in the section used for autoradiography. NFTs with few plaques were observed in the hippocampal CA2 region (**d**), while classic and compact plaques (*white arrow*) with dense cores coexisted with NFTs in the subiculum (**e**). In the parahippocampal gyrus (**f**), NFTs were abundant in concurrence with diffuse plaques faintly illuminated with FSB (*red arrow*). The fusiform gyrus (**g**) was dominated by primitive plaques containing dystrophic neurites (*arrowheads*)

primitive plaques with FSB-positive neurites (Fig. 6g), accounting for the strong reactivity of [^{11}C]PIB with this region.

Discussion

While the SUVR values of [^{11}C]PIB were significantly larger in AD patients than in normal control subjects, no significant differences were observed between normal control subjects and AD patients in [^{18}F]FACT studies. In both [^{11}C]PIB and [^{18}F]FACT studies, nonspecific accumulation in white matter was observed, and this must hamper the quantitative analysis of cortical uptake of radiotracer due to the limited spatial resolution of the PET scanner. To remove the effects of white matter accumulation, $SUVR_{gray}$ values were calculated using gray and white matter images extracted from MR images according to the method developed by Müller-Gärtner et al. [29]. This partial volume correction technique was also originally used for estimation of cerebral blood flow per gray matter fraction in an ROI [30]. The $SUVR_{gray}$ values were larger in AD patients than in normal control subjects in both [^{11}C]PIB and [^{18}F]FACT studies. Since several radiotracers for amyloid imaging show the nonspecific accumulation in white matter [4, 7, 8, 18], such partial volume correction will be needed to estimate the deposition of amyloid senile plaques in cerebral cortices by PET. On the other hand, a recently developed radiotracer for amyloid deposits [^{11}C]AZD2184 which shows no conspicuous accumulation in white matter may not need such partial volume correction [10].

Although the $SUVR_{gray}$ values of [^{18}F]FACT were smaller than those of [^{11}C]PIB in AD patients, good correlations were observed in $SUVR_{gray}$ values between [^{11}C]PIB and [^{18}F]FACT studies, indicating the validity of [^{18}F]FACT as a radiotracer for amyloid imaging. Comparing $SUVR_{gray}$ images between [^{11}C]PIB and [^{18}F]FACT, relatively lower $SUVR_{gray}$ values of [^{11}C]PIB in distribution were observed in the parahippocampal gyrus and occipital cortex as compared with [^{18}F]FACT. Relatively higher $SUVR_{gray}$ values of

[^{11}C]PIB in distribution were also observed in the frontal and parietal cortices. A radiotracer for amyloid imaging, [^{11}C]BF227, has been considered to bind more preferentially to dense-cored amyloid deposition than [^{11}C]PIB [7]. [^{18}F]FACT has a structure similar to [^{11}C]BF227 and therefore it also binds more preferentially to dense-cored amyloid deposition [18]. If the cerebral cortical uptake of [^{11}C]PIB might be due to binding to both diffuse and dense-cored amyloid plaque [32], such regional differences in cerebral cortical uptake between [^{11}C]PIB and [^{18}F]FACT might be due to differences in regional distribution between diffuse and dense-cored amyloid plaque. In the present study, the autoradiographic and histochemical assays of postmortem AD brain sections also showed that [^{18}F]FACT signals were associated with classic (dense-cored/neuritic) and compact plaques, and diffuse plaques could be a source of moderate signals for [^{11}C]PIB. A histopathological study showed that diffuse amyloid plaques were not prominent in the occipital lobe as compared with the frontal and temporal lobes [33]. This might correspond to the relatively lower $SUVR_{gray}$ of [^{11}C]PIB in the occipital cortex as compared to that of [^{18}F]FACT observed in the present study.

It has been reported that synapse loss was accentuated within immature and mature plaques, but not within diffuse plaques [16]. Since [^{18}F]FACT might bind more preferentially to dense-cored amyloid plaques, [^{18}F]FACT binding might be an indicator of the severity of AD. In the present study, significant positive correlations were observed between MMSE scores and $SUVR_{gray}$ of [^{18}F]FACT in many of the neocortical regions, but not in [^{11}C]PIB as also shown in previous studies [34]. Although the number of the subjects is rather small to investigate the correlation between MMSE scores and $SUVR_{gray}$, this indicates that cortical accumulation of [^{18}F]FACT can reflect the severity of AD to a greater extent than [^{11}C]PIB.

In conclusion, deposition of amyloid senile plaques was measured by PET with both [^{11}C]PIB and [^{18}F]FACT in the same subjects, including normal control subjects, MCI patients, and AD patients. After partial volume correction to remove the effects of white matter accumulation, cerebral cortical uptake was larger in AD patients than in normal control subjects in both [^{11}C]PIB and [^{18}F]FACT studies. Regional differences in cerebral cortical uptake were observed between [^{11}C]PIB and [^{18}F]FACT, possibly due to differences in regional distribution between diffuse and dense-cored amyloid plaques.

Acknowledgments This study was supported in part by "Japan Advanced Molecular Imaging Program (J-AMP)" of the Ministry of Education, Culture, Sports, Science and Technology (MEXT), Japanese Government, a Grant-in-Aid for Comprehensive Research on Dementia (No. 11103404) from the Ministry of Health, Labour and Welfare, and a Grant-in-Aid from the Mitsubishi Pharma Research Foundation. We thank Mr. Katsuyuki Tanimoto and Mr. Takahiro Shiraishi for their assistance in performing the PET experiments at the National Institute of Radiological Sciences. We also thank Ms. Kazuko Suzuki and Ms. Izumi Izumida of the National Institute of Radiological Sciences for their help as clinical research coordinators.

Conflicts of interest None.

References

1. Braak H, Braak E. Neuropathological stageing of Alzheimer-related changes. Acta Neuropathol 1991;82:239–59.
2. Hardy JA, Higgins GA. Alzheimer's disease: the amyloid cascade hypothesis. Science 1992;256:184–5.
3. Mathis CA, Wang Y, Holt DP, Huang GF, Debnath ML, Klunk WE. Synthesis and evaluation of 11C-labeled 6-substituted 2-arylbenzothiazoles as amyloid imaging agents. J Med Chem 2003;46:2740–54.
4. Klunk WE, Engler H, Nordberg A, Wang Y, Blomqvist G, Holt DP, et al. Imaging brain amyloid in Alzheimer's disease with Pittsburgh Compound-B. Ann Neurol 2004;55:306–19.
5. Agdeppa ED, Kepe V, Liu J, Flores-Torres S, Satyamurthy N, Petric A, et al. Binding characteristics of radiofluorinated 6-dialkylamino-2-naphthylethylidene derivatives as positron emission tomography imaging probes for beta-amyloid plaques in Alzheimer's disease. J Neurosci 2001;21:RC189.
6. Ono M, Wilson A, Nobrega J, Westaway D, Verhoeff P, Zhuang ZP, et al. 11C-labeled stilbene derivatives as Abeta-aggregate-specific PET imaging agents for Alzheimer's disease. Nucl Med Biol 2003;30:565–71.
7. Kudo Y, Okamura N, Furumoto S, Tashiro M, Furukawa K, Maruyama M, et al. 2-(2-[2-Dimethylaminothiazol-5-yl]ethenyl)-6-(2-[fluoro]ethoxy)benzoxazole: a novel PET agent for in vivo detection of dense amyloid plaques in Alzheimer's disease patients. J Nucl Med 2007;48:553–61.
8. Rowe CC, Ackerman U, Browne W, Mulligan R, Pike KL, O'Keefe G, et al. Imaging of amyloid beta in Alzheimer's disease with 18F-BAY94-9172, a novel PET tracer: proof of mechanism. Lancet Neurol 2008;7:129–35.
9. Choi SR, Golding G, Zhuang Z, Zhang W, Lim N, Hefti F, et al. Preclinical properties of 18F-AV-45: a PET agent for Aβ plaques in the brain. J Nucl Med 2009;50:1887–94.
10. Nyberg S, Jönhagen ME, Cselényi Z, Halldin C, Julin P, Olsson H, et al. Detection of amyloid in Alzheimer's disease with positron emission tomography using [11C]AZD2184. Eur J Nucl Med Mol Imaging 2009;36:1859–63.
11. Cselényi Z, Jönhagen ME, Forsberg A, Halldin C, Julin P, Schou M, et al. Clinical validation of 18F-AZD4694, an amyloid-beta-specific PET radioligand. J Nucl Med 2012;53:415–24.
12. Buckner RL, Snyder AZ, Shannon BJ, LaRossa G, Sachs R, Fotenos AF, et al. Molecular, structural, and functional characterization of Alzheimer's disease: evidence for a relationship between default activity, amyloid, and memory. J Neurosci 2005;25:7709–17.
13. Engler H, Forsberg A, Almkvist O, Blomquist G, Larsson E, Savitcheva I, et al. Two-year follow-up of amyloid deposition in patients with Alzheimer's disease. Brain 2006;129:2856–66.
14. Rowe CC, Ng S, Ackermann U, Gong SJ, Pike K, Savage G, et al. Imaging β-amyloid burden in aging and dementia. Neurology 2007;68:1718–25.
15. Wang J, Dickson DW, Trojanowski JQ, Lee VM. The levels of soluble versus insoluble brain Aβ distinguish Alzheimer's disease from normal and pathologic aging. Exp Neurol 1999;158:328–37.

16. Masliah E, Terry RD, Mallory M, Alford M, Hansen LA. Diffuse plaques do not accentuate synapse loss in Alzheimer's disease. Am J Pathol 1990;137:1293–7.
17. Price JL. Diagnostic criteria for Alzheimer's disease. Neurobiol Aging 1997;18:S67–70.
18. Furumoto S, Okamura N, Furukawa K, Tashiro M, Ishikawa Y, Sugi K, et al. A 18F-labeled BF-227 derivative as a potential radioligand for imaging dense amyloid plaques by positron emission tomography. Mol Imaging Biol 2013;15:497–506.
19. Shidahara M, Tashiro M, Okamura N, Furumoto S, Furukawa K, Watanuki S, et al. Evaluation of the biodistribution and radiation dosimetry of the 18F-labelled amyloid imaging probe [18F]FACT in humans. EJNMMI Res 2013;3:32.
20. McKhann G, Drachman D, Folstein M, Katzman R, Price D, Stadlan EM. Clinical diagnosis of Alzheimer's disease: report of the NINCDS-ADRDA Work Group under the auspices of Department of Health and Human Services Task Force on Alzheimer's Disease. Neurology 1984;34:939–44.
21. Morris JC. The Clinical Dementia Rating (CDR): current version and scoring rules. Neurology 1993;43:2412–4.
22. Folstein MF, Folstein SE, McHugh PR. "Mini-mental state". A practical method for grading the cognitive state of patients for the clinician. J Psychiatr Res 1975;12:189–98.
23. Matsumoto K, Kitamura K, Mizuta T, Tanaka K, Yamamoto S, Sakamoto S, et al. Performance characteristics of a new 3-dimensional continuous-emission and spiral-transmission high-sensitivity and high-resolution PET camera evaluated with the NEMA NU 2-2001 standard. J Nucl Med 2006;47:83–90.
24. Ishikawa A, Kitamura K, Mizuta T, Tanaka K, Amano M, Inoue Y, et al. Implementation of on-the-fly scatter correction using dual energy window method in continuous 3D whole body PET scanning. IEEE Nucl Sci Symp Conf Rec 2005;5:2497–500.
25. Price JC, Klunk WE, Lopresti BJ, Lu X, Hoge JA, Ziolko SK, et al. Kinetic modeling of amyloid binding in humans using PET imaging and Pittsburgh Compound-B. J Cereb Blood Flow Metab 2005;25:1528–47.
26. Ito H, Hietala J, Blomqvist G, Halldin C, Farde L. Comparison of the transient equilibrium and continuous infusion method for quantitative PET analysis of [11C]raclopride binding. J Cereb Blood Flow Metab 1998;18:941–50.
27. Friston KJ, Frith CD, Liddle PF, Dolan RJ, Lammertsma AA, Frackowiak RS. The relationship between global and local changes in PET scans. J Cereb Blood Flow Metab 1990;10:458–66.
28. Ashburner J, Friston KJ. Voxel-based morphometry–the methods. Neuroimage 2000;11:805–21.
29. Müller-Gärtner HW, Links JM, Prince JL, Bryan RN, McVeigh E, Leal JP, et al. Measurement of radiotracer concentration in brain gray matter using positron emission tomography: MRI-based correction for partial volume effects. J Cereb Blood Flow Metab 1992;12:571–83.
30. Ito H, Inoue K, Goto R, Kinomura S, Taki Y, Okada K, et al. Database of normal human cerebral blood flow measured by SPECT: I. Comparison between I-123-IMP, Tc-99m-HMPAO, and Tc-99m-ECD as referred with O-15 labeled water PET and voxel-based morphometry. Ann Nucl Med 2006;20:131–8.
31. Higuchi M, Iwata N, Matsuba Y, Sato K, Sasamoto K, Saido TC. 19F and 1H MRI detection of amyloid beta plaques in vivo. Nat Neurosci 2005;8:527–33.
32. Ikonomovic MD, Klunk WE, Abrahamson EE, Mathis CA, Price JC, Tsopelas ND, et al. Post-mortem correlates of in vivo PiB-PET amyloid imaging in a typical case of Alzheimer's disease. Brain 2008;131:1630–45.
33. Yamaguchi H, Hirai S, Morimatsu M, Shoji M, Harigaya Y. Diffuse type of senile plaques in the brains of Alzheimer-type dementia. Acta Neuropathol 1988;77:113–9.
34. Jack Jr CR, Lowe VJ, Senjem ML, Weigand SD, Kemp BJ, Shiung MM, et al. 11C PiB and structural MRI provide complementary information in imaging of Alzheimer's disease and amnestic mild cognitive impairment. Brain 2008;131:665–80.

Please cite this article in press as: Maruyama et al., Imaging of Tau Pathology in a Tauopathy Mouse Model and in Alzheimer Patients Compared to Normal Controls, Neuron (2013), http://dx.doi.org/10.1016/j.neuron.2013.07.037

Imaging of Tau Pathology in a Tauopathy Mouse Model and in Alzheimer Patients Compared to Normal Controls

Masahiro Maruyama,[1,10] Hitoshi Shimada,[1,10] Tetsuya Suhara,[1] Hitoshi Shinotoh,[1] Bin Ji,[1] Jun Maeda,[1] Ming-Rong Zhang,[1] John Q. Trojanowski,[2] Virginia M.-Y. Lee,[2] Maiko Ono,[1] Kazuto Masamoto,[1] Harumasa Takano,[1] Naruhiko Sahara,[3,5,6] Nobuhisa Iwata,[4] Nobuyuki Okamura,[7] Shozo Furumoto,[7] Yukitsuka Kudo,[8] Qing Chang,[9] Takaomi C. Saido,[4] Akihiko Takashima,[3] Jada Lewis,[5,6] Ming-Kuei Jang,[9] Ichio Aoki,[1] Hiroshi Ito,[1] and Makoto Higuchi[1,*]

[1]Molecular Imaging Center, National Institute of Radiological Sciences, 4-9-1 Anagawa, Inage-ku, Chiba, Chiba 263-8555, Japan
[2]Center for Neurodegenerative Disease Research, University of Pennsylvania Perelman School of Medicine, Third Floor HUP-Maloney, 36th and Spruce Streets, Philadelphia, PA 19104, USA
[3]Laboratory for Alzheimer's Disease
[4]Laboratory for Proteolytic Neuroscience
RIKEN Brain Science Institute, 2-1 Hirosawa, Wako, Saitama 351-0198, Japan
[5]Center for Translational Research in Neurodegenerative Disease
[6]Department of Neuroscience
University of Florida, 1275 Center Drive, Gainesville, FL 32610, USA
[7]Department of Pharmacology, Tohoku University Graduate School of Medicine, 2-1 Seiryo-machi, Aoba-ku, Sendai, Miyagi 980-8575, Japan
[8]Clinical Research, Innovation and Education Center, Tohoku University Hospital, 1-1 Seiryo-machi, Aoba-ku, Sendai, Miyagi 980-8574, Japan
[9]Institute for Applied Cancer Science, MD Anderson Cancer Center, 1901 East Road, Houston, TX 77054, USA
[10]These authors contributed equally to this work
*Correspondence: mhiguchi@nirs.go.jp
http://dx.doi.org/10.1016/j.neuron.2013.07.037

SUMMARY

Accumulation of intracellular tau fibrils has been the focus of research on the mechanisms of neurodegeneration in Alzheimer's disease (AD) and related tauopathies. Here, we have developed a class of tau ligands, phenyl/pyridinyl-butadienyl-benzothiazoles/benzothiazoliums (PBBs), for visualizing diverse tau inclusions in brains of living patients with AD or non-AD tauopathies and animal models of these disorders. In vivo optical and positron emission tomographic (PET) imaging of a transgenic mouse model demonstrated sensitive detection of tau inclusions by PBBs. A pyridinated PBB, [^{11}C]PBB3, was next applied in a clinical PET study, and its robust signal in the AD hippocampus wherein tau pathology is enriched contrasted strikingly with that of a senile plaque radioligand, [^{11}C]Pittsburgh Compound-B ([^{11}C]PIB). [^{11}C]PBB3-PET data were also consistent with the spreading of tau pathology with AD progression. Furthermore, increased [^{11}C]PBB3 signals were found in a corticobasal syndrome patient negative for [^{11}C]PIB-PET.

INTRODUCTION

Hallmark pathologies of Alzheimer's disease (AD) are extracellular senile plaques consisting of aggregated amyloid β peptide (Aβ) and intraneuronal neurofibrillary tangles (NFTs) composed of pathological tau fibrils, while similar tau lesions in neurons and glia are also characteristic of other neurodegenerative disorders, such as progressive supranuclear palsy (PSP) and corticobasal degeneration (CBD), that are collectively referred to as tauopathies (Ballatore et al., 2007). The discovery of *tau* gene mutations in a familial form of tauopathy, known as frontotemporal dementia and parkinsonism linked to chromosome 17 (FTDP-17), and subsequent studies of transgenic (Tg) mice expressing human tau with or without these mutations, clearly implicate pathological tau in mechanisms of neurodegeneration in AD and related tauopathies (Ballatore et al., 2007). Thus, there is an urgent need for tau imaging techniques to complement Aβ amyloid imaging methods that now are widely used.

In vivo imaging modalities, as exemplified by positron emission tomography (PET) (Klunk et al., 2004; Small et al., 2006; Kudo et al., 2007; Maeda et al., 2007), optical scanning (Bacskai et al., 2003; Hintersteiner et al., 2005), and magnetic resonance imaging (MRI) (Higuchi et al., 2005), have enabled visualization of Aβ deposits in humans with AD and/or AD mouse models, and there has been a growing expectation that low-molecular-weight ligands for β-pleated sheet structures will also serve as molecular probes for tau amyloids. Although the majority of plaque-imaging agents used for clinical PET studies do not bind to tau lesions (Klunk et al., 2003), at least one radiolabeled β sheet ligand, [^{18}F]FDDNP, enables PET imaging of AD NFTs (Small et al., 2006). However, a relatively low contrast of in vitro autoradiographic and in vivo PET signals for [^{18}F]FDDNP putatively reflecting tau lesions does not allow a simple visual inspection of images for the assessment of tau pathologies in living subjects

Please cite this article in press as: Maruyama et al., Imaging of Tau Pathology in a Tauopathy Mouse Model and in Alzheimer Patients Compared to Normal Controls, Neuron (2013), http://dx.doi.org/10.1016/j.neuron.2013.07.037

(Small et al., 2006; Thompson et al., 2009). Thus, better tau radioligands with higher affinity for tau fibrils and/or less nonspecific binding to tissues are urgently needed to complement high-contrast senile plaque imaging agents, including widely studied [^{11}C]Pittsburgh Compound-B ([^{11}C]PIB) (Klunk et al., 2004) and United States Food and Drug Administration-approved [^{18}F]florbetapir (Yang et al., 2012). In addition, [^{18}F]FDDNP and several other candidate tau probes do not bind to tau inclusions in non-AD tauopathy brains without plaque deposition (Okamura et al., 2005) and therefore can be clinically characterized only in AD patients with comingled Aβ and tau amyloids. Hence, compounds that detect diverse tau aggregates, including tau inclusions in non-AD neurodegenerative diseases and tau Tg models, could be used to interrogate in vivo interactions between exogenous ligands and tau pathologies.

Here, we found that the lipophilicity of β sheet ligands is associated with their selectivity for tau versus Aβ fibrils and that the core dimensions of these chemicals are major determinants of their reactivity with a broad spectrum of tau aggregates in diverse tauopathies and mouse models of tau pathology. Building on these observations, we developed a series of fluorescent compounds capable of detecting diverse tau lesions using optical and PET imaging in living Tg mouse models of tauopathies. Finally, we identified a radiotracer that produced the highest contrast for tau inclusions in animal PET and used it in exploratory in vivo imaging studies of AD patients, providing clear demonstration of signal intensification in tau-rich regions, in sharp distinction to [^{11}C]PIB-PET data reflecting plaque deposition.

RESULTS

Identification of PBBs as Ligands for Diverse Tau Inclusions in Human Tauopathies

We screened an array of fluorescent chemicals capable of binding to β sheet conformations (see the Compounds subsection in the Experimental Procedures). Fluorescence labeling with these compounds were examined in sections of AD brains bearing Aβ and tau amyloids (Figures 1A and 2A) and non-AD tauopathy brains characterized by tau inclusions and few or no Aβ plaques (Figure 2). Amyloid PET tracers currently used for human PET studies, PIB (Klunk et al., 2004), and BF-227 (Kudo et al., 2007), tightly bound to senile plaques, while they only weakly reacted with AD NFTs (Figures 1A; Figure S1 available online). PET probes reported to selectively label tau aggregates, BF-158 (Okamura et al., 2005) and THK523 (Fodero-Tavoletti et al., 2011), detected AD NFTs (Figures 2A and S1) but microscopically detectable fluorescence signals produced by FDDNP, which are presumed to bind to both Aβ and tau fibrils (Small et al., 2006), were consistent with dense cores of classic plaques and distinct from tau lesions (Figures 2A and S1). None of the above-mentioned PET ligands were reactive with tau inclusions in non-AD tauopathies, such as Pick bodies in Pick's disease (Figures 2A and S1) and neuronal and glial fibrillary lesions in PSP and CBD (data not shown). By contrast, these pathologies were intensely labeled with a widely used amyloid dye, thioflavin-S, and a derivative of another classic amyloid dye Congo red, (E,E)-1-fluoro-2,5-bis(3-hydroxycarbonyl-4-hydroxy)styrylbenzene (FSB) (Higuchi et al., 2005; Maeda et al., 2007) (Figures 1, 2A, and S1), although these chemicals may not undergo efficient transfer through the blood-brain barrier (BBB) (Zhuang et al., 2001). Because compounds possessing a π-electron-conjugated backbone longer than 13Å exhibited affinities for pathological inclusions in a broad range of tauopathies, we examined binding of additional chemicals with a variety of structural dimensions to tau aggregates and found that affinity for non-AD tau inclusions could be attributed to a core structure with a specific extent ranging from 13 to 19 Å (Figure S1). Based on this view and the known fact that chemicals with a flat and slender backbone could pass through and attach to channel-like accesses in β-pleated sheets (Krebs et al., 2005), we developed a class of compounds, phenyl/pyridinyl-butadienyl-benzothiazoles/benzothiazoliums (PBBs), by stretching the core structure of a prototypical fluorescent amyloid dye, thioflavin-T, with two C = C double bond inserts between aniline (or aminopyridine) and benzothiazole (or benzothiazolium) groups (Figure 1B).

All PBB compounds intensely labeled NFTs, neuropil threads, and plaque neurites in AD brains (Figure 1C). Interestingly, the affinity of these PBBs for Aβ plaques lacking dense cores was positively correlated with their lipophilicity (Figure 1C), and thereby three potential probes with relatively low logP (log of the octanol/water partition coefficient) values, including PBB3, 2-[4-(4-methylaminophenyl)-1,3-butadienyl]-benzothiazol-5,6-diol (PBB4) and PBB5 (structurally identical to Styryl 7, CAS registry number 114720-33-1), appeared suitable for visualizing tau pathologies in living organisms with reasonable selectivity. High-affinity of PBBs for tau lesions was further demonstrated by fluorometric analyses using Aβ and tau filaments assembled in a test tube (Table S1; experimental procedures are given in the Supplemental Experimental Procedures), but the most and least lipophilic PBB members displayed similar selectivity for in vitro tau versus Aβ pathologies, implying a methodological limitation in screening chemicals for tau-selective ligands based on binding to synthetic peptides and recombinant proteins. PBBs and FSB were also shown to label tau inclusions in non-AD tauopathies, such as Pick's disease (Figures 2A and S1), PSP, and CBD (Figure 2B), all of which were immunodetected by an antibody specific for phosphorylated tau proteins (AT8).

In Vitro and Ex Vivo Fluorescence Imaging of Tau Lesions in Tau Tg Mice by PBBs

To obtain in vivo evidence of direct interaction between PBBs and tau lesions, we employed Tg mice expressing a single human four-repeat tau isoform with the P301S FTDP-17 mutation (PS19 line, see Figure S2 for neuropathological features of this Tg strain) (Yoshiyama et al., 2007). Similar to the findings in non-AD tauopathy brains, NFT-like inclusions in the brain stem and spinal cord of PS19 mice were clearly recognized by PBBs (Figures 3A and S1). We then performed ex vivo labeling of tau lesions in PS19 mice with intravenously administered, fluorescently labeled PBBs. Brains and spinal cords were removed 60 min after tracer injection, and fluorescence microscopy revealed an intense accumulation of these compounds in fibrillary tau inclusions abundantly seen throughout the sections by

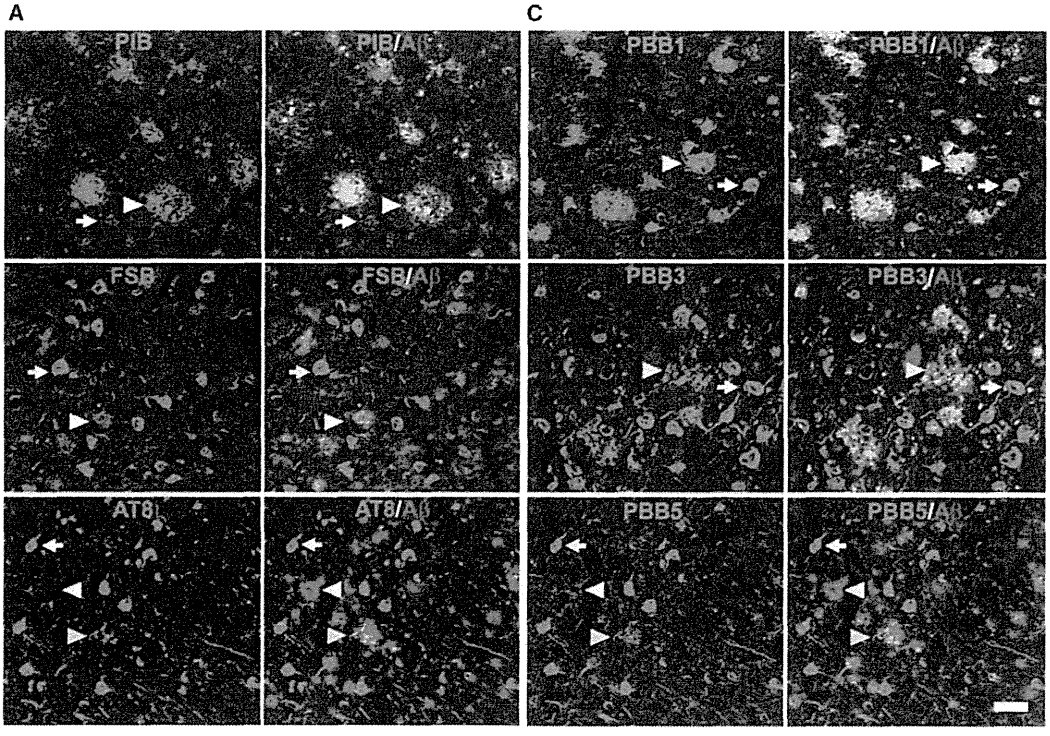

B

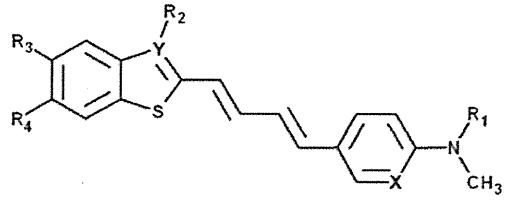

Compound	R_1	R_2	R_3	R_4	X	Y	ClogP
PBB1	CH_3	-	H	H	C(H)	N	5.44
PBB2	H	-	H	OH	C(H)	N	3.57
PBB3	H	-	H	OH	N	N	3.30
PBB4	H	-	OH	OH	C(H)	N	2.97
PBB5	CH_3	CH_3CH_2	H	H	C(H)	N^+	2.32

Figure 1. Design and Characterization of PBB Compounds as Potential Imaging Agents for Tauopathies

(A) Confocal fluorescence images of frontal cortex sections from an AD patient. Following fluorescence labeling (pseudocolors are converted to green) with PIB (top row) and FSB (middle row), the samples were immunostained with an antibody against AβN3(pE) (red in the right column). PIB intensely labeled Aβ plaques (white arrowheads) but did not clearly label NFTs (arrows). By contrast, NFTs and neuropil threads were intensely labeled by FSB, whereas the staining of diffuse plaques was negligible. A section was also doubly immunolabeled (bottom row) with AT8 (green) and anti-AβN3(pE) antibodies (red in the right panel), to demonstrate the abundance of tau and Aβ amyloids in this area. Yellow arrowheads indicate tau-positive dystrophic neurites associated with senile plaques.

(B) Structures of PBBs. Neutral benzothiazoles (PBB1-4) are newly synthesized chemicals, and a charged benzothiazolium, PBB5, is identical to a commercially available near-infrared laser dye.

(C) Confocal fluorescence images of PBBs (pseudocolors are converted to green) and AβN3(pE) (red in the right column) staining in sections adjacent to those displayed in (A). The intensity of plaque staining (arrowheads) relative to that of NFTs (arrows) was positively associated with the lipophilicity of PBBs. As compared with PBB1 (top row) staining, labeling of diffuse plaques with PBB3 (middle row) was substantially attenuated. PBB5 was nearly unreactive with diffuse plaques (bottom row), and subsequent double immunofluorescence staining of the same section (bottom row in C) illustrated good agreement of PBB5 labeling with the distribution of AT8-positive NFTs.

Scale bar, 50 μm (A and C). See also Figure S1 and Table S1.

staining with thioflavin-S, FSB, and AT8 (Figure 3B). On the other hand, no overt in vitro (Figure 3A) or ex vivo (data not shown) fluorescence of these ligands was noted in the corresponding regions of non-Tg wild-type (WT) mice. Consistent with these observations, two-photon laser scanning fluorescence microscopy of ex vivo samples demonstrated somatic and neuritic staining of a subset of tangle-bearing neurons with intravenously injected 2-[4-(4-methylaminophenyl)-1,3-butadienyl]-benzothiazol-6-ol (PBB2) and PBB4 in unsliced spinal cord blocks from PS19 mice (Figure 3B).

In Vivo Macroscopic and Mesoscopic Optical Detection of Fibrillar Tau Pathologies in a Mouse Model Using PBB5

We next characterized PBBs with the use of in vivo fluorescence imaging modalities, which permitted a quick assessment of

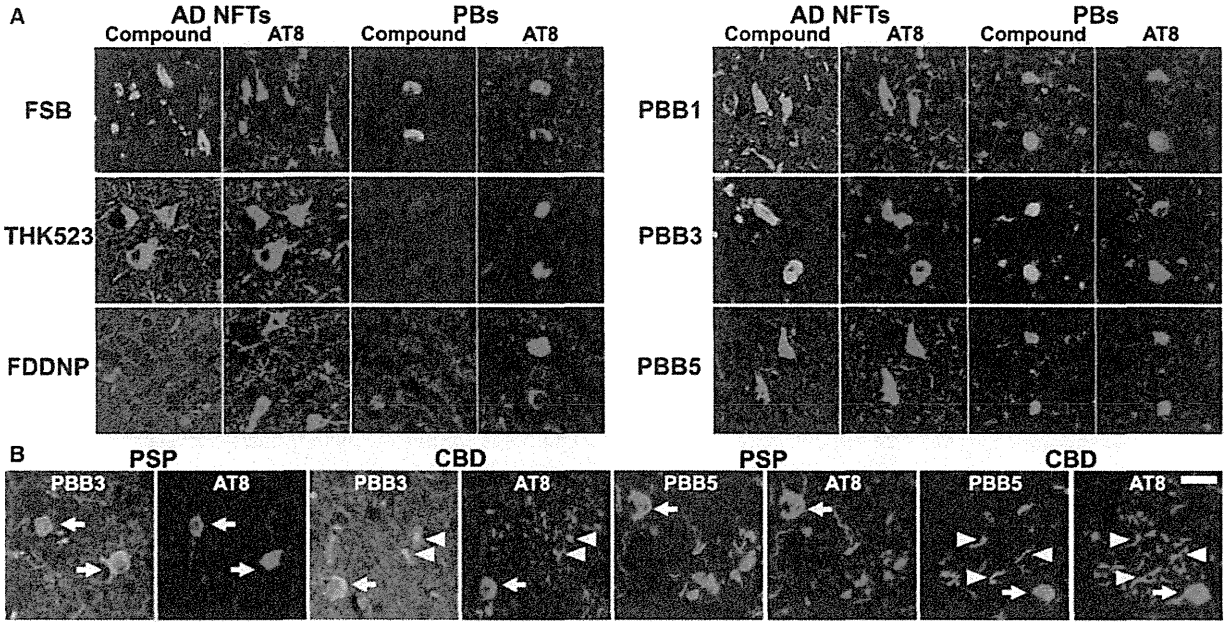

Figure 2. Binding of Tau Ligands to Tau Lesions in AD and Non-AD Tauopathy Brains

(A) Double fluorescence staining of AD NFTs and Pick bodies (PBs) in Pick's disease with PBBs, other tau ligands, and anti-phospho-tau antibody (AT8). FSB and PBBs sensitively captured AD NFTs and PBs. AD NFTs were labeled with THK523. Meanwhile, PBs were not visualized by these compounds. NFTs and PBs were barely recognizable by using FDDNP.

(B) Double fluorescence staining of neuronal tau inclusions (arrows) in PSP and CBD and putative astrocytic plaques (arrowheads) in CBD. A substantial portion of tau fibrils in neurons were captured by PBB3 and PBB5, but a much smaller subset of phosphorylated tau aggregates in astrocytic plaques were labeled with these compounds.

Scale bar, 20 μm (A and B). See also Figures S2 and S3.

candidate chemicals without the need for radiolabeling. Because PBB5 is fluorescent, with peak excitation and emission wavelengths in a near-infrared range (Table S1), this compound is applicable to in vivo optical imaging of tau deposits in laboratory animals. To examine this possibility, fluorescence images were obtained from living mice over a time course following intravenous PBB5 injections using a small animal-dedicated system permitting the intravital observation of fluorescence signals at magnifications varying between macroscopic and microscopic levels. Tail vein administration of PBB5 in PS19 mice revealed strong fluorescence relative to non-Tg WT mice in the central nervous system (CNS) above the slit between the base of the skull and first vertebra, through the skin and connective tissues overlaying the cisterna magna (Figures S3A–S3D), suggesting a concentration of this tracer in the PS19 spinal cord. In line with this in vivo observation, the hindbrain and spinal cord of PS19 mice, which were dissected out at 2 hr after the injection of PBB5, exhibited increased retention of this compound compared to non-Tg WT mice (Figures S3E–S3G).

In vivo optical imaging of tau Tg mice was subsequently performed using a device equipped with a pulsed diode laser and a photomultiplier tube to detect deep signals through the skull. Elevated levels of fluorescence intensity were found in homogenized brain stem samples collected from PS19 mice at 20 hr after the intravenous tracer administration (Figure S4A), indicating a long-lasting in vivo binding of PBB5 to tau fibrils. To support the ex vivo evidence, fluorescence intensity was noninvasively analyzed in living PS19 and non-Tg WT mice treated with PBB5. The mice, with their heads shaved in advance, were prescanned, and autofluorescence signals were detected at a relatively high level in an area corresponding to the frontal forebrain. Using these baseline signals as landmarks, regions of interest (ROIs) were defined in the frontal cortex, brain stem, and spinal cord (Figure 4A). The near-infrared fluorescence was notably increased immediately after the intravenous injection of PBB5 (Figure S4C), and the fluorescence in the brain stem and spinal cord ROIs of PS19 mice much exceeded that in WT mice at 30 min (Figure 4B). Fluorescence intensity in the frontal cortex ROI, normalized on the basis of integration time and laser power, was lower in PS19 mice than in WT mice over 120 min after tracer injection (Figure S4B), which may reflect impaired CNS delivery of the tracer in Tg mice due to degenerative changes (see Figures S4C–S4L for details), and thereafter this became almost equivalent between the two genotypes (Figure S4B). Meanwhile, persistent retention of the signals in the brain stem and spinal cord ROIs of PS19 mice was observed beyond 240 min (Figures 4B and S4B). A more quantitative index comparable among different mice was determined by calculating the target-to-frontal-cortex ratio of fluorescence intensity and was shown to increase over time particularly in PS19 mice (Figures 4C and 4D). This ratio was significantly greater in PS19 mice than in WT mice at 240 min (Figure 4E), beyond which the difference

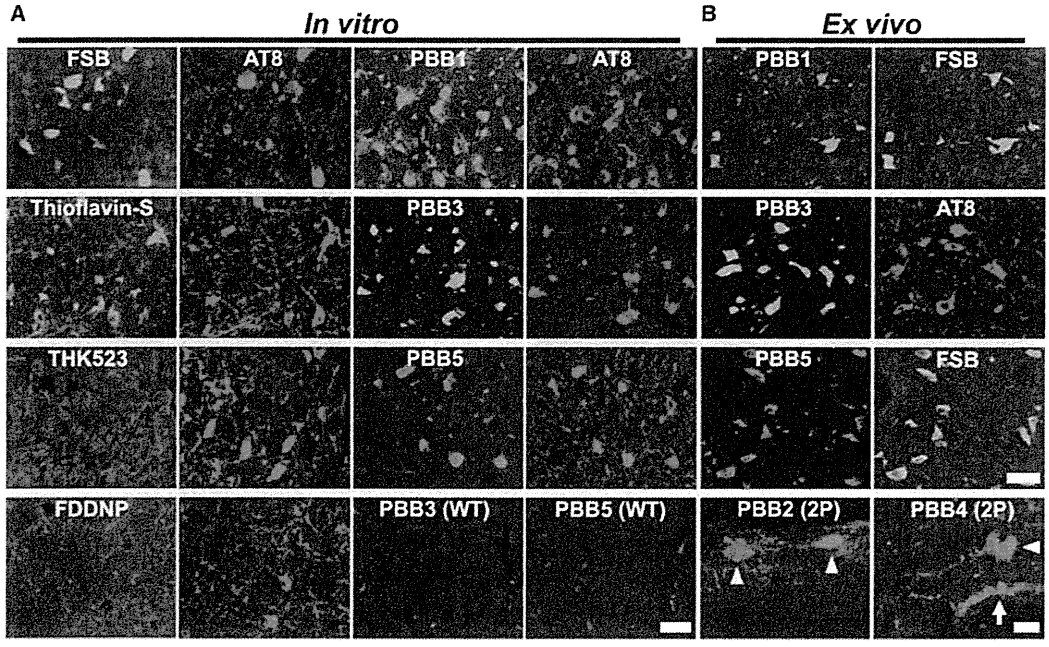

Figure 3. In Vitro and Ex Vivo Labeling of NFTs in PS19 Mice with PBB Compounds

(A) Double fluorescence staining of intraneuronal tau aggregates in postmortem brain stem slices of a 12-month-old PS19 mouse with PBB, other amyloid ligands, and anti-phospho-tau antibody (AT8).

(B) Binding of intravenously administered PBBs (0.1 mg/kg PBB5 and 1 mg/kg PBB1 and PBB3) to NFTs in PS19 mice at 10–12 months of age. The tissues were sampled at 60 min after tracer administration. The brain stem (top row) and spinal cord (second and third rows from the top) sections abundantly contained neurons showing strong fluorescence (left), and subsequent staining with FSB or AT8 (right) indicated that these cells were laden with tau amyloid fibrils (right). Putative intraneuronal tau inclusions in unsectioned spinal cords (arrowheads in the bottom row) removed from PS19 mice at 60 min after intravenous injection of PBB2 and PBB4 were also clearly visible by using a two-photon (2P) fluorescence microscopic system. Arrow in the bottom row indicates a cluster of autofluorescence signals from blood cells.

Scale bars, 25 μm (A), 30 μm (top to third rows in B), and 20 μm (bottom row in B).

between the two lines of mice became nearly constant (Figures 4C and 4D). The intensity ratio of the spinal cord ROI to the frontal cortex in PS19 mice at 240 min was also significantly correlated with the abundance of NFTs stained with FSB (Figure 4F), but such correlations were not statistically significant in the brain stem (Figure 4F), implying limitations of the intensitometry in some brain regions below the cerebellum and fourth ventricle.

Intravital Imaging of Individual Tau Inclusions by PBB3 and Two-Photon Laser Scanning Fluorescence Microscopy

Two-photon excitation microscopy, which enables optical sectioning, potentially up to 1 mm deep, in living tissues, could be utilized to visually demonstrate transfer of a fluorescent probe from the plasma compartment into the cytoplasm of CNS neurons and binding of the probe to intraneuronal tau inclusions. We therefore captured fluorescence signals from intravenously administered PBB3 by in vivo two-photon laser scanning microscopic imaging of the spinal cord of laminectomized PS19 mice. Within 3 s of PBB3 injection, green fluorescence signals emerged in blood vessels prelabeled with red with intraperitoneal treatment using sulforhodamine 101 and subsequently diffused from the vasculatures to the spinal cord parenchyma over the next few minutes (Figures 5A–5F). These diffuse signals declined thereafter due to the clearance of PBB3 from the tissue, whereas intense labeling of putative tau inclusions with green fluorescence appeared in a subpopulation of large cells morphologically identified as neurons at 3–5 min after PBB3 injection (Figures 5G and 5H). These intracellular PBB3 fluorescent signals were not found in the spinal cord of WT mice (Figure 5I). As the BBB of the brain and spinal cord are presumed to be identical, the two-photon microscopic data obtained here provide compelling evidence that PBB3 rapidly transits the BBB and neuronal plasma membranes, where it binds to intraneuronal tau inclusions. Accumulation of injected PBB3 in AT8-positive, NFT-like lesions of Tg mice was postmortemly confirmed by ex vivo microscopy (Figures 5J and 5K).

Autoradiographic and PET Imaging of Tau Lesions in PS19 Mice by Radiolabeled PBBs

We investigated the kinetic properties of PBBs by high-performance liquid chromatography (HPLC) analyses of plasma and brain samples collected from non-Tg WT mice treated with these ligands. Following intravenous administration, PBB5 was rapidly converted into a major metabolite, which at 5 min was found at high levels in both plasma and brain extracts. Subsequent liquid

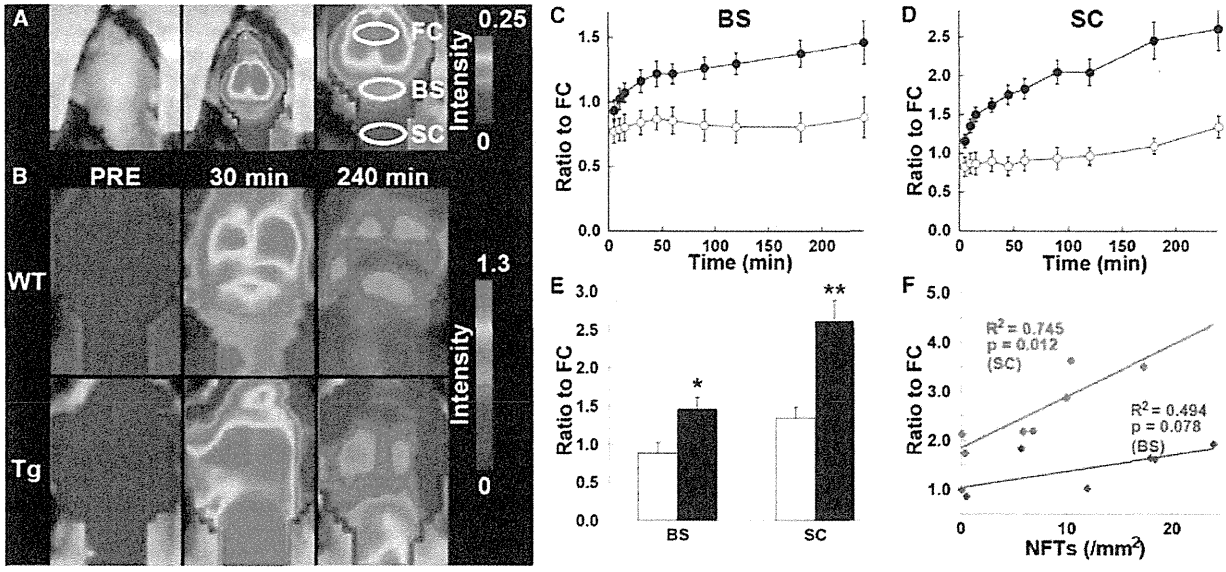

Figure 4. Noninvasive Near-Infrared Imaging of Tau Pathology in Living Tau Tg Mice Using Pulsed Laser Optics and PBB5

(A) Baseline autofluorescence signals (middle) are overlaid on the visible background image of a shaven non-Tg WT mouse head (left). Ellipsoidal ROIs are defined above the frontal cortex (FC), brain stem (BS), and cervical spinal cord (SC) guided by a relatively intense emission from the FC region (right).

(B) Fluorescence intensity maps in 12-month-old WT (top) and PS19 (Tg; bottom) mice before and at 30 and 240 min after the intravenous administration of PBB5 (0.1 mg/kg). The intensity maps (A and B) are normalized by the FC ROI value at 30 min after tracer injection. Long-lasting retention of the tracer was noted in the BS and SC ROIs of the Tg mouse.

(C and D) Target-to-FC ratios of fluorescence intensity in the BS (C) and SC (D) ROIs over the image acquisition time in the WT (open circles; n = 7) and PS19 (closed circles; n = 7) mice. There were significant main effects of time, region, and genotype in two-way, repeated-measures ANOVA (time, $F_{(11, 132)} = 17.6$, $p < 0.001$; region, $F_{(1, 12)} = 29.9$, $p < 0.001$; genotype, $F_{(1, 12)} = 23.6$, $p < 0.001$).

(E) Target-to-FC ratios in the BS and SC ROIs of the WT (open columns) and tau Tg (closed columns) mice at 240 min after tracer injection. $^*p < 0.05$; $^{**}p < 0.01$; two-way repeated-measures ANOVA with Bonferroni's post hoc analysis.

(F) Scatterplots of target-to-FC ratios at 240 min versus the number of FSB-positive NFTs per unit area of postmortem 20 μm tissue slices in BS (blue symbols) and SC (red symbols) ROIs of tau Tg mice. Solid lines represent regressions; p values were determined by t test. Vertical bars in the graphs represent SEs.

See also Figures S3 and S4.

chromatography-mass spectrometry (LC-MS) assays suggested that the major metabolite was likely a reduced, electrically neutralized derivative of PBB5 (Figures S5A and S5B). Besides transventricular uptake of unmetabolized PBB5 as implied above, this uncharged form incapable of emitting near-infrared light could readily penetrate the BBB, as well as cell membranes, and thereafter could be reoxidized into its original form, thereby enabling it to bind to tau fibrils, particularly at sites exposed to oxidative stress in pathological conditions. In addition, PBB4 was promptly converted to metabolites capable of entering the brain. Finally, studies of PBB2 and PBB3 showed that they exhibited reasonable biostability and sufficient entry into and clearance from the brain. Indeed, HPLC assays demonstrated that fractions of unmetabolized PBB2 and PBB3 in mouse plasma were 23.5% and 16.3%, respectively, at 3 min after intravenous administration and were 4.6% and 2.8%, respectively, at 30 min. There were also no metabolites of PBB2 and PBB3 detectable in the mouse brain at 3 and 30 min.

We then radiolabeled PBB2 and PBB3 with ^{11}C to conduct autoradiographic and PET assays using PS19 mice. In vitro autoradiography using frozen tissue sections showed binding of these radioligands to the brain stem of PS19 mice and neocortex of AD patients (Figure 6A). As expected from their lipophilicities, [^{11}C]PBB3 yielded high-contrast signals with less nonspecific labeling of myelin-rich white matter than did [^{11}C]PBB2, and the accumulation of [^{11}C]PBB3 in pathological regions was nearly completely abolished by the addition of nonradioactive compounds. Similarly, ex vivo autoradiographic studies demonstrated that intravenously administered [^{11}C]PBB3 selectively labeled the brain stem and spinal cord of PS19 mice harboring neuronal tau inclusions, whereas tau-associated [^{11}C]PBB2 radiosignals were less overt because of a considerable level of nonspecific background (Figure 6B; Figures S6C–S6F). Finally, in vivo visualization of tau lesions in PS19 mouse brains was enabled by a microPET system using these two tracers (Figures 6C, S6A, and S6B). Following intravenous injection, [^{11}C]PBB3 rapidly crossed the BBB and unbound and nonspecifically bound tracers were promptly washed out from the brain with a half-life of ~10 min (left panel in Figure 6E). The retention of [^{11}C]PBB3 signals in the brain stem of 12-month-old PS19 mice lasted over the imaging time (90 min), producing a pronounced difference from that in age-matched non-Tg WT mice (left panel in Figure 6E). By selecting the striatum as a reference region lacking tau deposits, the target-to-reference ratio was estimated for the brain stem, with the value in PS19 mice peaking at around 70 min, contrasting with its continuous decrease over

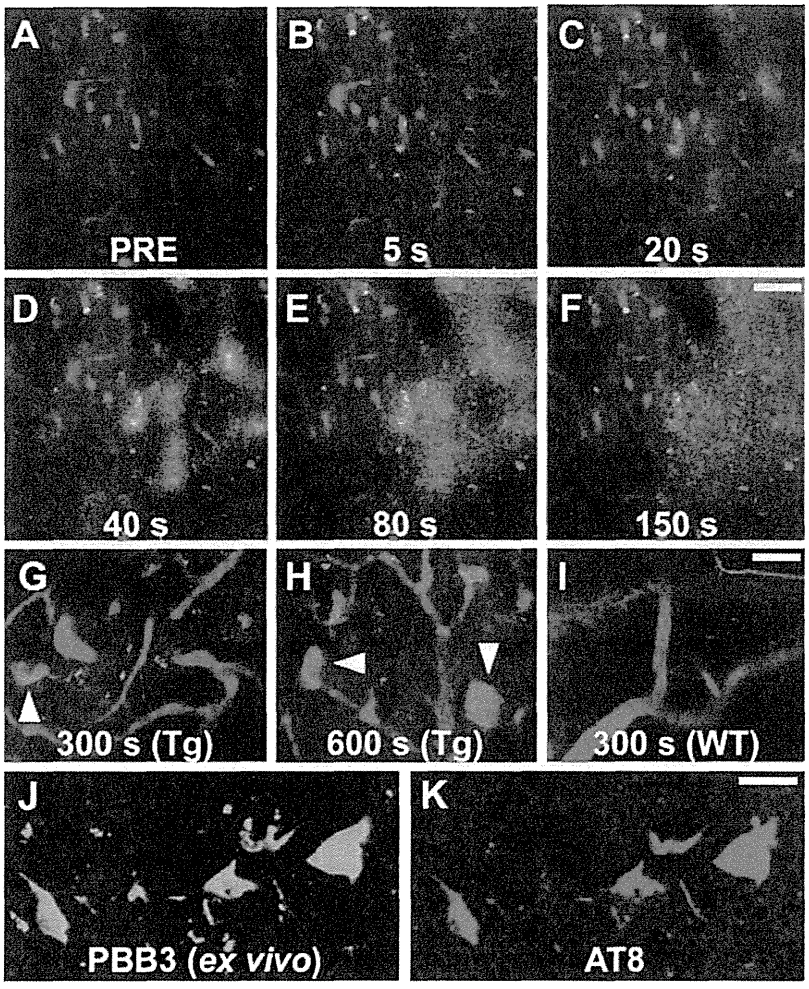

Figure 5. Real-Time Two-Photon Laser Scanning Images of PBB3 Diffusing from Vessels, Binding to Intraneuronal Tau Inclusions, and Clearing from Spinal Cord

(A–H) A maximum projection of fluorescence in a 3D volume of the spinal cord of a living PS19 mouse at 12 months of age before (A) and at various time points after (B–H) intravenous administration of PBB3 (1 mg/kg). Blood vessels were labeled with sulforhodamine 101 (red) intraperitoneally injected at 15 min before PBB3 administration. Green fluorescence indicates a rapid transfer of PBB3 from the plasma to tissue parenchyma (B–E) and subsequent washout from the tissue (F). Background PBB3 signals were further attenuated beyond 300 s, whereas somatodendritic labeling by this compound was observed in a subset of neurons (arrowheads in G and H).

(I) Fluorescence image of WT spinal cord at 300 s after PBB3 injection demonstrates no overt retention of the tracer in the tissue.

(J and K) Ex vivo microscopy for a brain stem section of the same Tg mouse. Tissues were obtained at 60 min after PBB3 injection. Signals of intravenously administered PBB3 (J) overlapped with AT8 immunoreactivity (K).

Scale bars, 50 μm (A–F), 25 μm (G–I), and 25 μm (J and K).

60 min in WT mice (right panel in Figure 6E). The mean ratio at 45–90 min was increased by 40% in 12-month-old PS19 mice as compared with age-matched WT mice ($p < 0.01$ by t test). The agreement between localizations of PET signals and tau inclusions in PS19 mice was proven by postmortem FSB staining of brain sections from scanned mice (Figure 6D). Significantly, the mean target-to-reference ratio in the brain stem quantified by PET correlated closely with the number of FSB-positive inclusions per brain section in the same region of the postmortem sample ($p < 0.001$ by t test; data not shown). [^{11}C]PBB2 exhibited slower clearance from the brain and higher nonspecific retention in myelin-rich regions than [^{11}C]PBB3 (Figure S6G), resulting in insufficient contrast of tau-bound tracers in the brain stem of PS19 mice and a small difference in the target-to-reference ratio of radioactivities between PS19 and WT mice (8% at 45–90 min; $p < 0.05$ by t test; Figure S6H) relative to those achieved with [^{11}C]PBB3.

As radiolabeling at the dimethylamino group in PBB5 with ^{11}C was unsuccessful, ^{11}C-methylation of a hydroxyl derivative of this compound was performed, leading to the production of [^{11}C]methoxy-PBB5 ([^{11}C]mPBB5; Figure S5C). PET images demonstrated complex pharmacokinetics of [^{11}C]mPBB5 (Figures S5D and S5E), and the difference in the specific radioligand binding between Tg and WT mice was small relative to the [^{11}C]PBB3-PET data (Figure S5F). After taking all of these findings into consideration, [^{11}C]PBB3 was selected as the most suitable ligand for in vivo PET imaging of tau pathology in tau Tg nice and human subjects.

Notably, the hippocampus of many PS19 mice was devoid of overt [^{11}C]PBB3 retention (Figure 6C), although a pronounced hippocampal atrophy was noted in these animals. This finding is in agreement with the well-known neuropathological features of PS19 mice in the hippocampus, because the accumulation of AT8-positive phosphorylated tau inclusions results in the degeneration of the affected hippocampal neurons prior to or immediately after NFT formation, followed by the clearance of their preNFTs or NFTs that are externalized into the interstitial CNS compartment (Figure S2). To explore the feasibility of our imaging agents in studies with other tauopathy model mice, we also performed fluorescence labeling with PBBs for brain sections generated from rTg4510 mice (Santacruz et al., 2005; the Supplemental Experimental Procedures). As reported elsewhere (Santacruz et al., 2005), these mice developed numerous thioflavin-S-positive neuronal tau inclusions in the neocortex and hippocampus, and reactivity of these lesions with PBBs was demonstrated by in vitro and ex vivo fluorescence imaging (Figure S7).

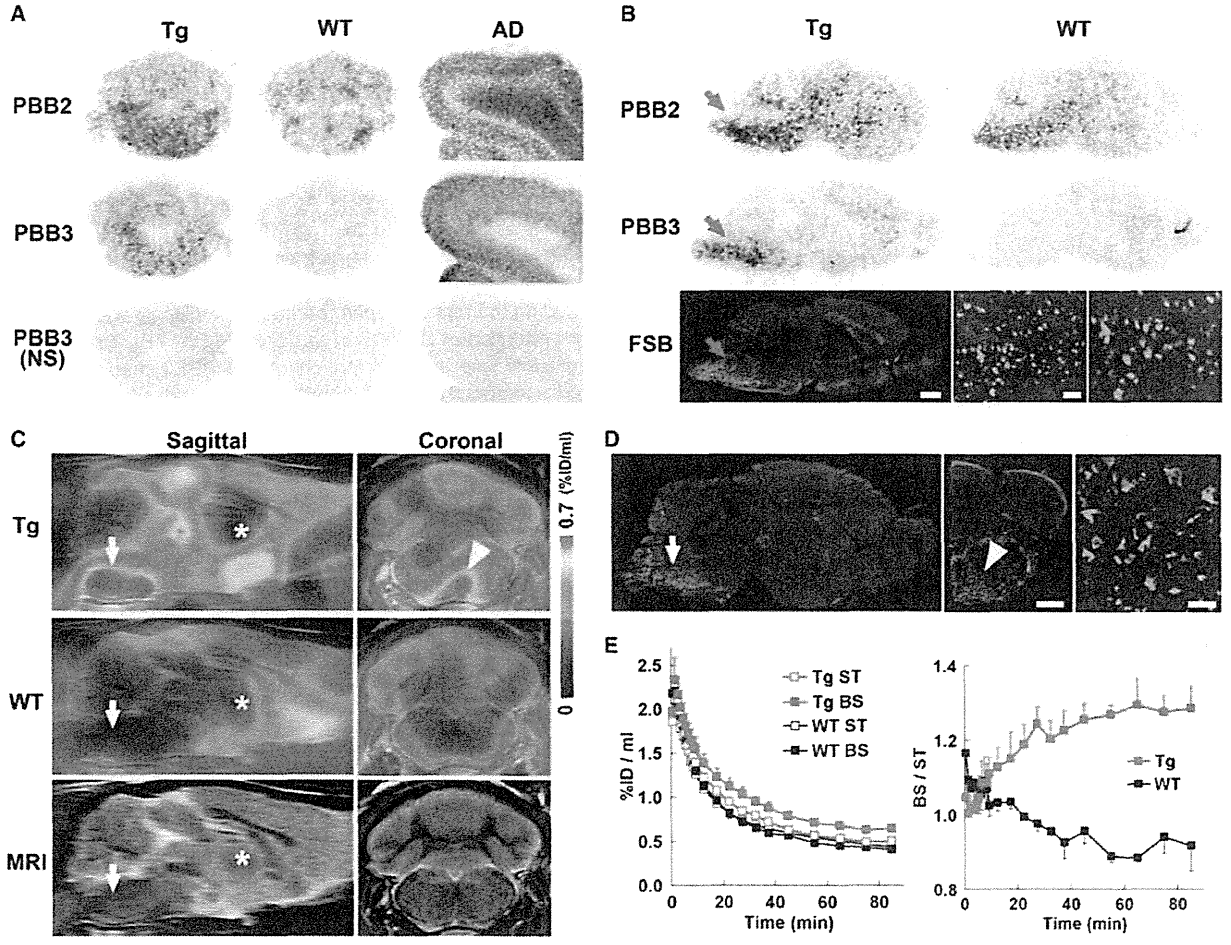

Figure 6. PET and Autoradiographic Detection of Tau Pathologies in PS19 Mice Using [^{11}C]PBB2 and [^{11}C]PBB3

(A) In vitro autoradiograms of PS19 and non-Tg WT hindbrains (coronal sections) and AD frontal cortex. Fibrillar aggregates in the mouse brain stem and AD gray matter produced intense radiolabeling with both tracers, but nonspecific background signals were also observed at a considerably high level with the use of [^{11}C]PBB2. Binding of [^{11}C]PBB3 was profoundly abolished by the addition of nonradioactive PBB3 (10 μM).

(B) Autoradiographic labeling with intravenously injected [^{11}C]PBB2 and [^{11}C]PBB3 in PS19 (Tg) and WT mice. The brains were removed at 45 min after injection and were cut into sagittal slices. The autoradiographic section of PS19 brain was also stained with FSB. Arrows indicate the brain stem containing numerous tau inclusions displayed at intermediate and high magnifications.

(C) Sagittal and coronal PET images generated by averaging dynamic scan data at 60–90 min after intravenous administration of [^{11}C]PBB3. The images are overlaid on the MRI template (images of the template alone are presented at the bottom). Arrows and asterisks indicate the brain stem and striatum, respectively, and arrowhead denotes intense radiolabeling in the medial brain stem of the PS19 mouse.

(D) FSB staining of PS19 mouse brain shown in (C). Sagittal (left) and coronal (middle) images and a high-power view of fibrillar inclusions (right) are displayed. Corresponding to high-level retention of [^{11}C]PBB3 in PET scans, abundant FSB-positive lesions were found in the medial brain stem (arrow and arrowhead).

(E) Time-radioactivity curves (left) in the striatum (ST) and brain stem (BS) and BS-to-ST ratio of radioactivity (right) over the imaging time in PS19 (Tg; red symbols) and WT (black symbols) mice (n = 5 each). Vertical bars in the graphs denote SEs.

Scale bars, 1 cm (A and B, top, middle, and bottom left panels); 1 cm (C and D, left and middle panels); 100 μm (B, bottom middle panel); and 100 μm (B, bottom right panel and D, right panel). See also Figures S5, S6, and S7.

Detection of Tau Pathologies in Living Brains of AD Patients by Comparative PET Imaging with [^{11}C]PBB3 and [^{11}C]PIB

In order to compare the bindings of [^{11}C]PBB3 and [^{11}C]PIB to tau-rich regions in the human brain, in vitro autoradiography was carried out with sections of AD and control hippocampus. A notable difference in labeling between these two radioligands was observed in the CA1 sector and subiculum of the AD hippocampus, where fibrillar tau aggregates predominantly localized to NFTs and neuropil threads (Figure 7A).

We subsequently conducted an exploratory clinical PET study for patients with probable AD (n = 3) and age-matched cognitively normal control (NC) subjects (n = 3). All AD patients exhibited a marked increase in the retention of [^{11}C]PIB in

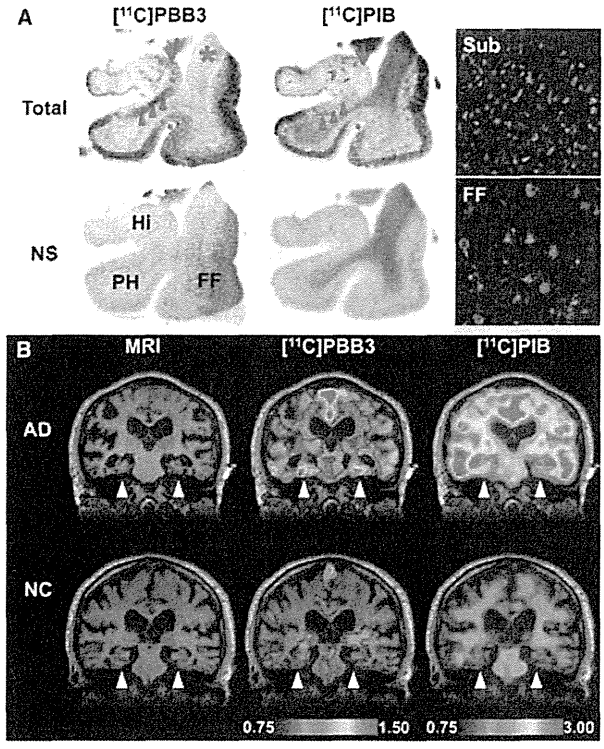

Figure 7. Accumulation of [^{11}C]PBB3 in the Hippocampal Formation of AD Patients Revealed by In Vitro Autoradiography and In Vivo PET

(A) Autoradiographic labeling of adjacent brain sections from an AD patient with 10 nM of [^{11}C]PBB3 (left) and [^{11}C]PIB (middle). The slices contain the hippocampus (Hi), parahippocampal gyrus (PH), fusiform gyrus (FF), and white matter (asterisks). Total binding (top) of [^{11}C]PBB3 and [^{11}C]PIB was markedly abolished (bottom) by addition of nonradioactive PBB5 (100 μM) and thioflavin-S (10 μM), respectively, except for the nonspecific (NS) labeling of white matter with [^{11}C]PIB. The hippocampal CA1 sector and subiculum displayed intense [^{11}C]PBB3 signals without noticeable binding of [^{11}C]PIB, and binding of [^{11}C]PBB3 in cortical areas flanking the collateral sulcus (identified by a red dot) and hippocampal CA2 sector (arrows) was also abundant relative to that of [^{11}C]PIB. FSB staining of amyloid fibrils in the sections used for autoradiography indicated the predominance of NFTs and diffuse plaques in the hippocampal subiculum (Sub) and fusiform gyrus (FF), respectively (right panels), supporting the strong reactivity of [^{11}C]PBB3 with AD NFTs.

(B) MRI (left) and PET imaging with [^{11}C]PBB3 (middle) and [^{11}C]PIB (right) performed in the same AD (top) and normal control (NC; bottom) subjects. Coronal images containing the hippocampal formation (arrowheads) are displayed. [^{11}C]PBB3- and [^{11}C]PIB-PET images were generated by estimating SUVRs at 30–70 min and 50–70 min after radiotracer injection, respectively, and were superimposed on individual MRI data. In the hippocampal formation, prominently increased retention of [^{11}C]PBB3 in the AD patient was in sharp contrast to the modest or negligible changes in [^{11}C]PIB binding as compared with NC. Scale ranges for SUVRs were 0.75–1.50 ([^{11}C]PBB3) and 0.75–3.00 ([^{11}C]PIB).

See also Figure S9.

plaque-rich areas, and all NC were negative for this PET assay. These subjects then received a [^{11}C]PBB3-PET scan, and the [^{11}C]PIB and [^{11}C]PBB3 images were compared in the same individuals. Intravenously injected [^{11}C]PBB3 was delivered to the brain tissue despite its relatively rapid metabolism in humans (Figures 9A and 9B). Unlike [^{11}C]PIB, [^{11}C]PBB3 showed minimal nonspecific binding to white matter and other anatomical structures with high myelin content, although it accumulated in dural venous sinuses in control and AD brains (Figures 7B, 8, and 9B). Time courses of regional radioactivity (Figures 9C and 9D; Figures S8A and S8B) and the standardized uptake value ratio (SUVR) to the cerebellum (Figures S8C and S8D) demonstrated accumulation of [^{11}C]PBB3 in several brain regions of AD patients as compared to controls (definition of these VOIs is indicated in Figure S8E). In agreement with autoradiographic findings, binding of [^{11}C]PBB3 to the medial temporal region, including the hippocampus, contrasted strikingly with the low-level retention of [^{11}C]PIB in this area (Figure 7B). There was a slight increase in the retention of [^{11}C]PBB3 primarily in the medial temporal region of a control subject with a loss of several points in Mini-Mental State Examination (MMSE) (subject 3 in Figure 8), appearing similar to the tau pathology at Braak stage III/IV or earlier (Braak and Braak, 1991), distinct from the lack of enhanced [^{11}C]PIB signals. Indeed, mild increase of medial temporal SUVR (Figure 9E) contrasted with unremarkable change in lateral temporal and frontal SUVRs in this subject (Figures 9G and 9H). Signals of [^{11}C]PBB3 were also intense mainly in the limbic region of a subject with early AD (subject 4 in Figure 8), but profound and moderate increases of SUVRs were also observed in the lateral temporal and frontal cortices, respectively, of this case (Figures 9G and 9H), resembling the localization of tau deposits at Braak stage V/VI (Braak and Braak, 1991). With the further cognitive decline as scored by MMSE (subjects 5 and 6 in Figure 8), additional increase in the retention of [^{11}C]PBB3 was found in the medial temporal region, precuneus, and frontal cortex (Figures 9E, 9F, and 9H). Meanwhile, a substantial decline of [^{11}C]PBB3 binding was noted in the lateral temporal cortex of subject 6 (Figures 8 and 9G). The SUVRs in the medial temporal region, precuneus, and frontal cortex were consequently well correlated with the decline of MMSE scores (Figures 9E, 9F, and 9H). In distinction with [^{11}C]PBB3-PET data, there was no overt association between the binding of [^{11}C]PIB and disease severity in AD patients (Figure 8), consistent with previous observations. These data support the potential utility of [^{11}C]PBB3 for clarifying correlations between the distribution of tau deposition and the symptomatic progression of AD.

As in vitro fluorescence staining indicated that PBB3 was reactive with not only tau lesions but also several types of senile plaques, particularly dense core plaques, density of binding sites, and affinity of [^{11}C]PBB3 for these sites were quantified by autoradiographic binding assays with hippocampal and neocortical sections of AD brains enriched with NFTs and senile plaques, respectively. These analyses demonstrated that specific radioligand binding sites were primarily constituted by high-affinity, low-capacity binding components in NFT-rich regions and low-affinity, high-capacity binding components in plaque-rich regions (Figures S9A and S9B). A subsequent simulation for radioligand binding in an area containing these two types of binding sites at a ratio of 1:1 indicated that the selectivity of [^{11}C]PBB3 for NFTs versus plaques may be inversely associated with concentration of free radioligands (Figure S9C). In a range of free concentration in the brain achievable

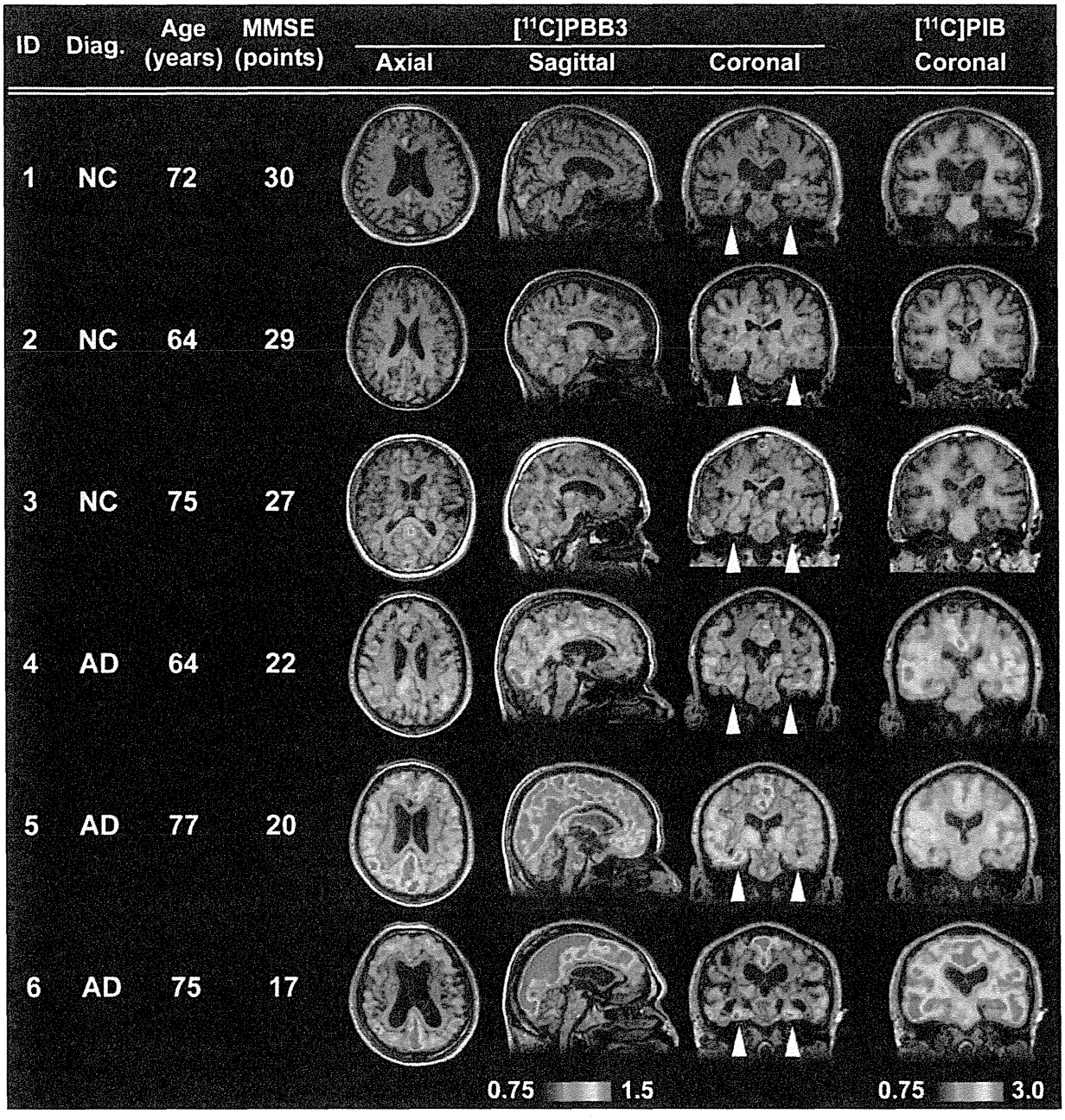

Figure 8. Orthogonal [^{11}C]PBB3-PET Images in All Human Subjects Examined in the Present Exploratory Clinical Study

Data are displayed as parametric maps for SUVR. The [^{11}C]PBB3 binding to the hippocampal formation (arrowheads) was increased consistently in AD patients in contrast to minimum radiotracer retention in normal control (NC) subjects with MMSE scores of 29–30 points (subjects 1 and 2). Another NC subject with an MMSE score of 27 points (subject 3) was negative for [^{11}C]PIB-PET but exhibited slight accumulation of radiotracer signals primarily around the hippocampus, resembling fibrillar tau deposition at Braak stage III/IV or earlier. Sagittal slices around the midline illustrate that radioligand signals were the most intense in the limbic system but began to expand to the neocortex in a patient with the mildest AD (subject 4), in agreement with the tau pathology at Braak stage V/VI, and was further intensified in most neocortical areas, corresponding to Braak stage VI, apparently as a function of the disease severity assessed by MMSE (subjects 5 and 6). The AD patient with the lowest MMSE score (subject 6) displayed a less profound increase of [^{11}C]PBB3 retention in the lateral temporal and parietal cortices than did the other two AD cases, and this is attributable to marked cortical atrophy in this individual and/or toxic loss of tau-bearing neurons in these brain areas at an advanced pathological stage. In contrast to the spatial profiles of [^{11}C]PBB3 binding, the distribution of [^{11}C]PIB signals appeared unchanged among AD subjects. See also Figure S9.

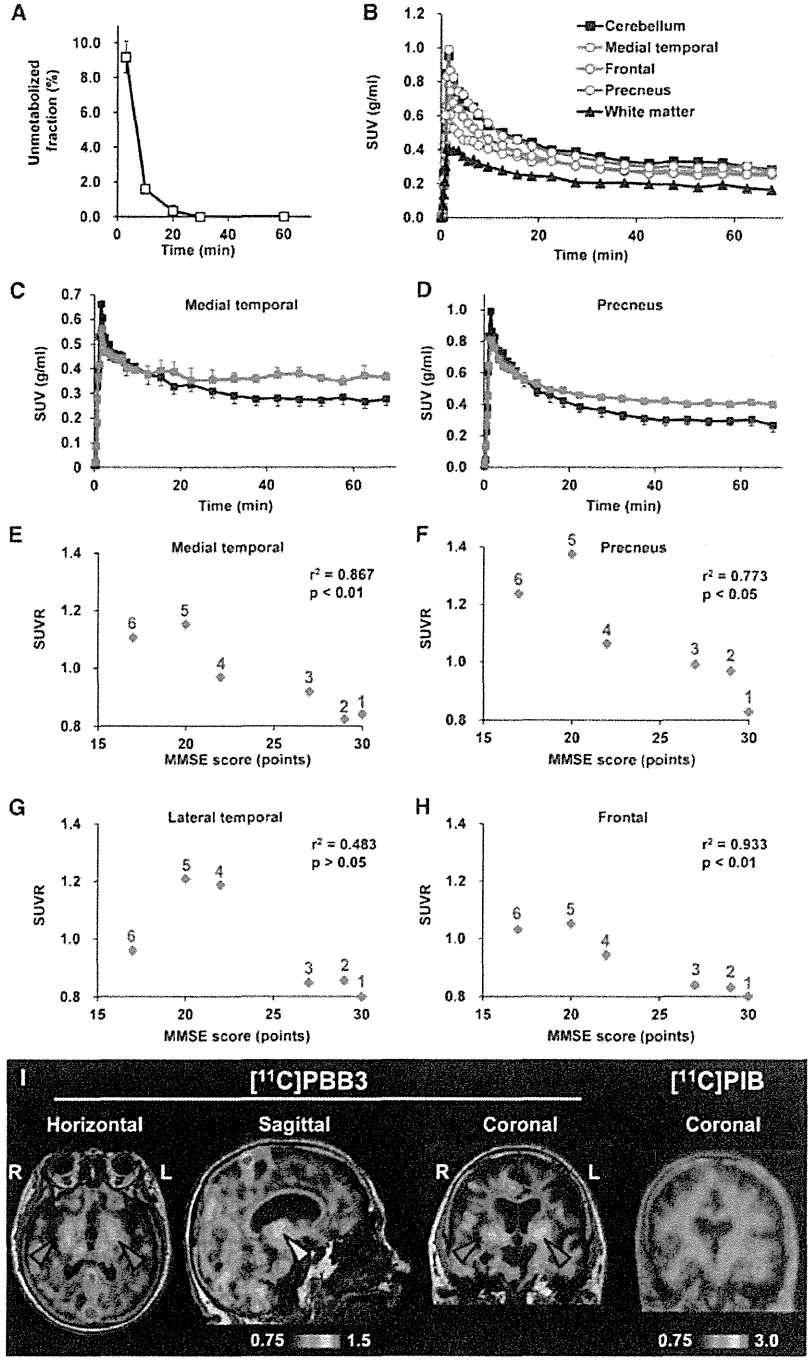

Figure 9. Pharmacokinetic Profiles of [^{11}C]PBB3 Administered to Humans and PET Images of a Patient Clinically Diagnosed as Having Corticobasal Syndrome

(A) Time course of unmetabolized [^{11}C]PBB3 fraction in plasma following intravenous radiotracer injection. The plot was generated by averaging data from six individuals.

(B) Time-radioactivity curves in different brain regions of cognitively normal control subjects over 70 min after intravenous injection of [^{11}C]PBB3. Data were generated by averaging values in two individuals and are presented as standard uptake values (SUVs).

(C and D) Comparisons of time-radioactivity curves in the medial temporal region (C) and precuneus (D) of normal controls (black symbols and lines; n = 3) and AD patients (red symbols and lines; n = 3).

(E–H) Scatterplots illustrating correlation of SUVRs with MMSE scores in the medial temporal region (E), precuneus (F), and lateral temporal (G) and frontal (H) cortices. Numbers beside symbols denote subject ID as indicated in Figure 8. Coefficients of determination (r^2) and p values by t test are displayed in graphs.

(I) [^{11}C]PBB3- and [^{11}C]PIB-PET images in a subject with clinical diagnosis of corticobasal syndrome. Images were generated as in Figures 7 and 8. Accumulation of [^{11}C]PBB3 was noticeable in the basal ganglia (red arrowheads) with right-side dominance and an area containing the thalamus and midbrain (yellow arrowhead).

Vertical bars in the graphs represent SEs. See also Figures S8 and S9.

at a pseudoequilibrium state in human PET imaging (<0.2 nM), [^{11}C]PBB3 is presumed to preferentially bind to tau lesions relative to in vitro autoradiographic (~1 nM) and fluorescence (>100 nM) labeling.

We also estimated contribution of [^{11}C]PBB3 bound to dense core plaques to total radiosignals in the neocortical gray matter of AD patients, by conducting autoradiography and FSB histochemistry for the same sections. Radiolabeling associated with dense cored plaques accounted for less than 1% and 3% of total gray matter signals in the temporal cortex and precuneus, respectively (Figures S9D–S9H). Moreover, fluorescence labeling of adjacent sections with PBB3 demonstrated that approximately 2% and 5% of total gray matter fluorescence signals were attributable to PBB3 bound to dense core plaques in the temporal cortex and precuneus, respectively. Hence, dense cored plaques were conceived to be rather minor sources of binding sites for [^{11}C]PBB3.

Finally, PET scans with [^{11}C]PBB3 and [^{11}C]PIB were conducted for a subject clinically diagnosed as having corticobasal syndrome. Retention of [^{11}C]PIB stayed at a control level, but notable accumulation of [^{11}C]PBB3 was observed in the neocortex and subcortical structures (Figure 9I), providing evidence for in vivo detection of tau lesions in plaque-negative